Chapter 5
Caisson Failure Induced by Liquefaction: Barcelona Harbour, Spain

TABLE OF CONTENTS

5.1 Building a Caisson Dyke 87
5.2 The Failure 88
5.3 Soil Conditions 91
5.3.1 Liquefaction 96
5.4 Settlement Records and Their Interpretation 100
5.5 Safety During Caisson Sinking 103
5.5.1 Caisson weight 103
5.5.2 Bearing capacity 104
5.5.3 An upper bound solution for a rough strip footing founded on clay with a linearly increasing strength with depth 106
5.6 Caisson Consolidation. Increase in Soil Strength 110
5.6.1 Stress increments under a strip footing and determination of excess pore pressures 110
5.6.2 Stress increments 111
5.6.3 Initial excess pore pressures 112
5.6.4 Excess pore pressure dissipation 113
5.6.5 Effective stresses and updated undrained strength 119
5.7 Caisson Full Weight. Safety Factor Against Failure and Additional Consolidation 119
5.7.1 Caissons under full weight 121
5.8 Caissons Under Storm Loading 124
5.8.1 Wave forces on caissons 124
5.8.2 Static analysis. Safety factor 125
5.8.3 Analysis of liquefaction 128
5.9 Discussion 136
5.10 Mitigation Measures 139
5.10.1 Increasing the consolidation time under caisson weight 139
5.10.2 Increasing the size of the granular berm 140
5.10.3 Improving foundation soils 140
5.10.4 Increasing caisson width 140
5.10.5 After the failure 140
5.11 Lessons Learned 140
5.11.1 Foundation on normally consolidated soft soil 140
5.11.2 Strength changes due to caisson loading 141

A.M. Puzrin et al., *Geomechanics of Failures*, DOI 10.1007/978-90-481-3531-8_5,

5.11.3 Undrained vs drained analysis....141
5.11.4 Evolution of undrained strength....141
5.11.5 Spatial distribution of c_u controls mode of failure....141
5.11.6 Type of loading and the failure mechanism....142
5.11.7 Alternative definitions of safety factor....142
5.11.8 Defining soil liquefaction conditions....142
5.11.9 Simplified analysis of liquefaction....142
5.11.10 The flexibility of upper bound calculation....143
5.11.11 Failure mechanism....143
5.12 Advanced Topics....143
Appendix 5.1 Hydrodynamic Loads on Caisson....144
References....146

Chapter 5

Caisson Failure Induced by Liquefaction: Barcelona Harbour, Spain

5.1 Building a Caisson Dyke

The design of a new entrance for the Barcelona harbour involved opening a channel through the existing dyke and the protection of the opening by means of a new dyke made of reinforced concrete caissons (Fig. 5.1).

Caissons (each 19.6 m wide, 19.5 m high and 33.75 m long) were built in a mobile platform and towed to their intended position, shown in Figure 5.1. Caissons have a cellular structure. Inner vertical concrete walls allow filling the caisson in a controlled manner. In this way, the caisson may be precisely sunk (by controlled inundation of cells). Once "in situ", the total weight is increased by sand filling the caisson cells. Caisson foundation design should ensure stability against caisson weight and wave loading.

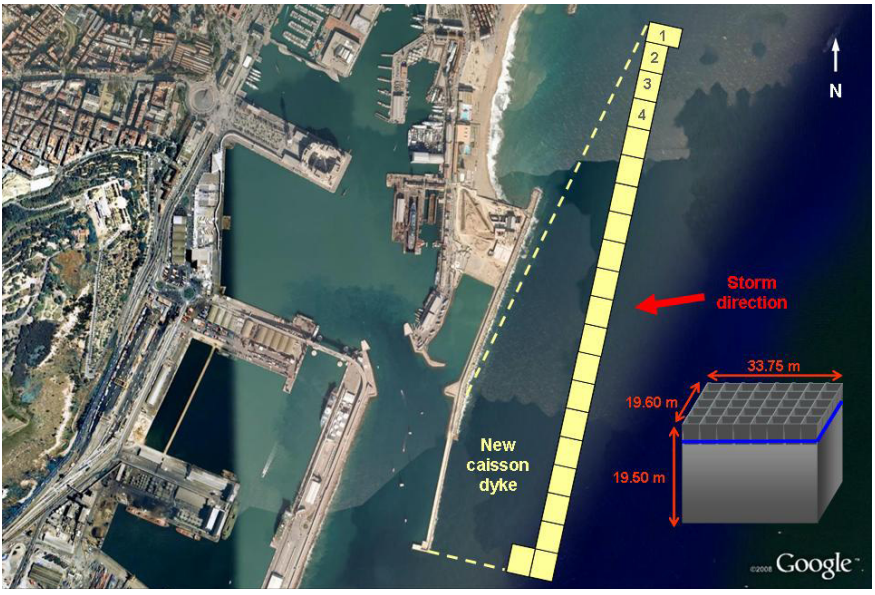

Figure 5.1 The new caisson breakwater (background photograph from Google Earth).

Foundation soils were deposited during the development of two overlapping deltas (Besós river delta towards the north-east and Llobregat river delta towards the south-west of the site). Soft silts and silty clays extend from the surface to substantial depths (tens of meters). A band close to the coastline is covered by a mantle of sand whose thickness decreases towards the sea.

The deep soft soils in the Barcelona harbour area are a challenge for caisson stability. The favoured design is to substitute part of the natural soils by a frictional fill extending on both sides of the breakwater (sea side and land side). Figure 5.2 shows a sketch of the foundation conditioning. A dredged trench is first excavated. Coarse granular soils are then backfilled and a final gravelly layer is leveled in preparation for caisson sinking.

Once sunk in place, caissons are finally capped with a concrete slab and a protective wall is built to avoid wave overrunning. It will be shown later that the vertical average net stress of the caissons filled with sand against the foundation soils is of the order of 220 kPa.

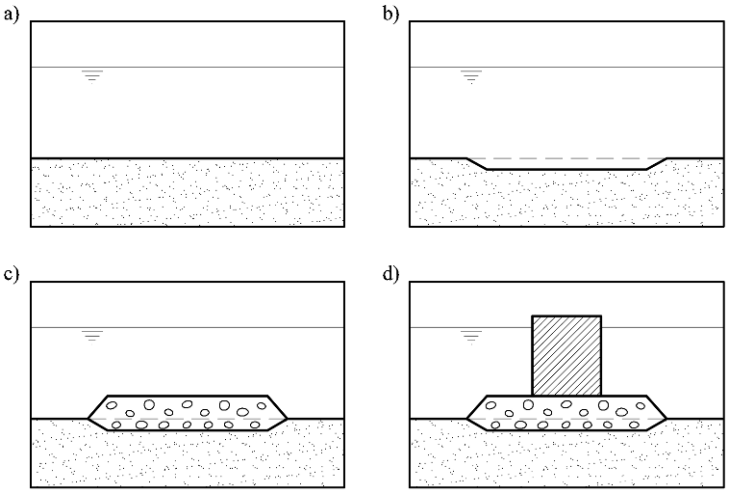

Figure 5.2 Caisson construction sequence: (a) initial soil conditions; (b) trench excavation; (c) extension of granular embankment; (d) caisson sinking.

5.2 The Failure

Dredging of the trench prepared to receive the coarse granular fill was finished on November 2000. Trench filling took the following six months. On May 10, 2001 the granular base was levelled and ready for the sinking of four caissons, in the position shown in Figure 5.1 (Caissons 1, 2, 3 and 4). Caisson sinking began, however, in the middle of October 2001. Cells were filled with sand some days later.

On November 10, 2001 an east-northeast storm with maximum significant wave heights of 4 m hit the coast. The time record of wave period and significant height is given in Figure 5.3. Some time during the night of November 10 and November 11, the four caissons failed. Figure 5.4 shows an aerial view of the failure. The two central caissons are not in sight and the extreme ones are seen to be tilted and partially submerged.

This failure was not a good starting experience for a breakwater typology which began to be used in the Barcelona harbour area, known for its soft

foundation soils. The traditional and successful design was the embankment type of breakwater. The failure teaches, however, an important lesson to geotechnical engineers: the risk involved in moving ahead of standard well-proven engineering practices and entering into new ground, into a "terra incognita".

Let us examine first the failure in more detail.

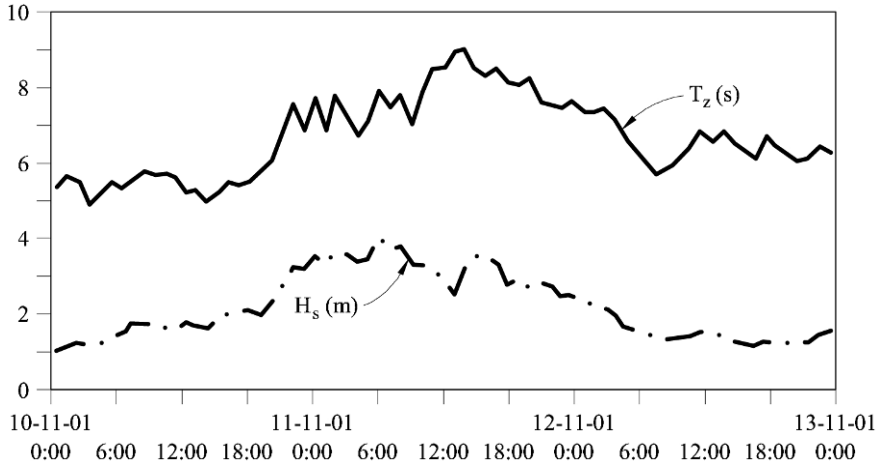

Figure 5.3 Significant wave heights (H_s) and wave period (T_z) of the storm.

Figure 5.4 Failed caissons.

The recorded maximum wave period was 9 seconds. The maximum intensity of the storm in terms of significant wave height (H_s = 4 m) lasted around one hour and therefore the number of wave load applications during this time interval was around 250 – 350. However, the precise failure time is unknown.

Soil profiles were established after the failure. They could be compared with the sea bottom topography before the works and immediately before caisson installation. Such a comparison is given in Figure 5.5 for a cross-section of Caisson 3 (one of the central caissons). The original and final positions of the caisson are also plotted.

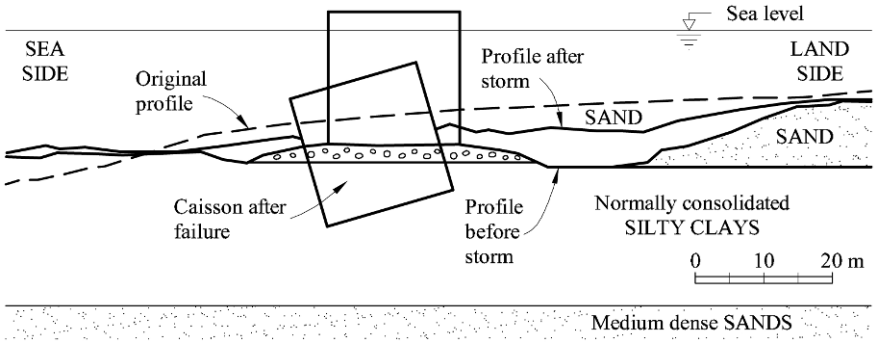

Figure 5.5 Cross-section through Caisson 3 before and after failure. Also shown is the original soil profile, the excavated profile, the granular berm, and the soil profile after the failure.

The caisson is deeply buried into the soil. The tilt of caisson top, towards the open sea, is consistent with a bearing capacity type of instability induced by an inclined load (the resultant of caisson self-weight and wave loading).

The caisson volume below the soil surface is estimated in Figure 5.5 to be 240 m^3/m. The depth of burial suggests that the foundation soil could have liquefied. This aspect will be examined later. The internal caisson walls were severely damaged. Wall reinforcement was not intended to resist the efforts associated with a large tilt.

The four caissons involved in the failure were later covered by a conventional fill-type breakwater. However, the remaining caissons envisaged in the project were built after a revision of the foundation design. They provided settlement data, shown later, which helps to derive some foundation parameters (average stiffness and consolidation coefficient).

The profiles given in Figure 5.5 indicate that the initial excavation in sands, in the land direction, was substantially filled again after the caisson failure. The calculated soil volume between the surface profiles before and after the storm is around 220 m^3/m, a value which is very similar to the buried caisson volume under the foundation level. It is then reasonable to accept that the caisson failure displaced the foundation soil towards the land side following a deep failure surface. It is also inferred that wave action after the caisson failure distributed the volume of soil initially displaced by the caisson failure over a wider area.

5.3 Soil Conditions

Figure 5.6 shows a simplified representative stratigraphic profile under caissons. An upper layer of loose silty sand, 10 meters thick, overlies a deposit of clayey silts and silty clays, 20 m thick. Below, a level of medium to dense sands was found. The upper 9 m of sands were removed by dredging. It appears that the thickness of the coarse granular fill below the caisson was rather small (around 2 m). The figure also shows the estimated lateral extent of the coarse granular embankment in the land direction. A detailed stratigraphic record with additional information on soil parameters derived from a few undisturbed samples tested is given in Figure 5.7. The figure also includes SPT N values.

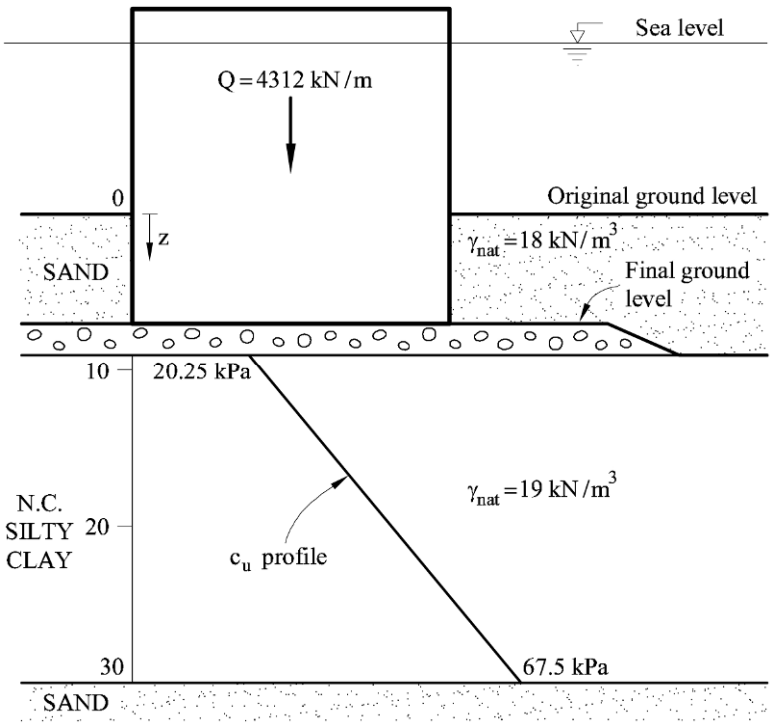

Figure 5.6 Simplified soil profile under caissons.

The silty clay is a soft deposit as revealed by the low N values (9, 4, 4, 5, 13…). It has a moderate plasticity (w_L= 30 – 32.6%) and the Plasticity Index is particularly low (4 – 10%). These deltaic deposits classify as ML, CL-ML or CL. The void ratio is high: 0.92 – 0.96.

Figure 5.8 shows an oedometric compression curve of a specimen recovered at a depth of 12.50 m below the soil surface. If normally consolidated, the vertical yield or preconsolidation stress would be around 12.50 m × 8 kN/m^3 = 100 kPa. This is close to the value found in the oedometer test using a classical construction shown in the figure. It is concluded that the silt deposit is normally consolidated.

The calculated virgin compression coefficients (C_c= 0.22 – 0.26) are high.

The coefficient of consolidation determined in small specimens is of limited reliability. The settlement records of the caissons built later will be analyzed below to determine this parameter and to estimate the permeability "in situ". The lower silty sands and clean sands are markedly stiffer. This is reflected in the high SPT values (N = 15 to 46), in the lower void ratio (e = 0.7) and in the small compressibility index, C_c = 0.06, measured in an oedometer test on a recovered sample.

Unconfined compression strengths, measured in samples (12 – 19 kPa), remain below the minimum accepted values for a normally consolidated low plasticity deposit, a result which may be explained by sample disturbance.

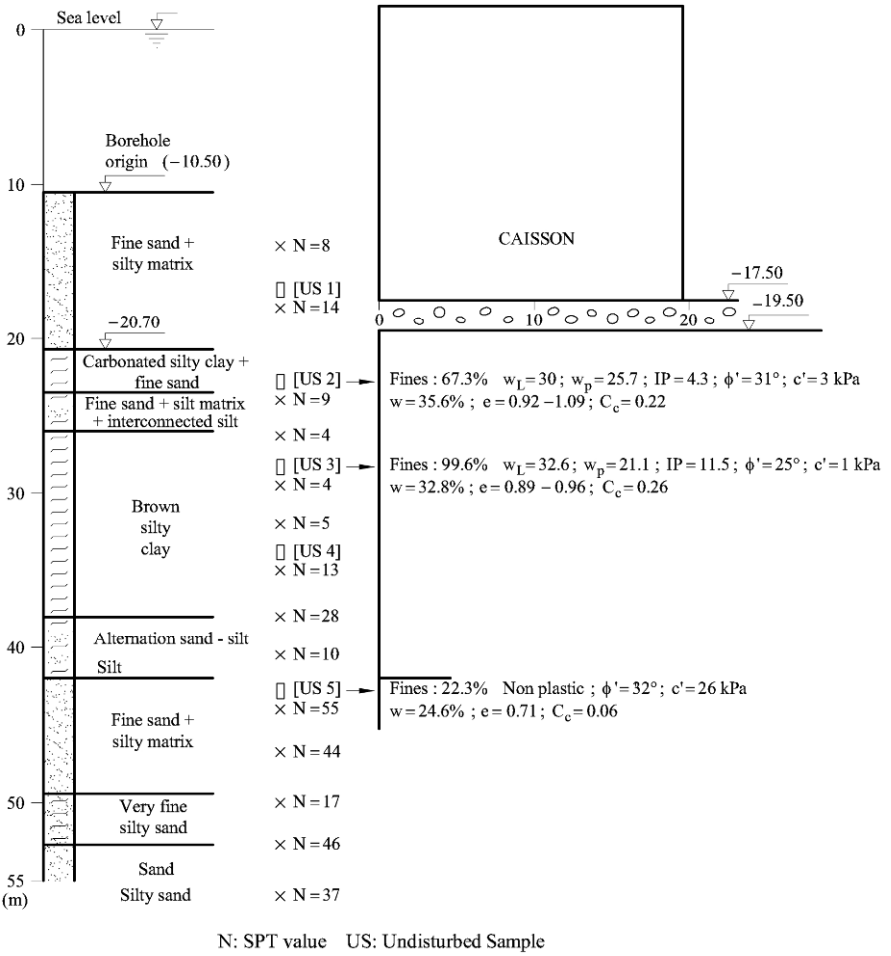

Figure 5.7 Detailed soil profile under caissons.

The undrained strength of normally consolidated soils increases with the confining effective stress. A useful relationship is

$$c_u = a\sigma'_v, \tag{5.1}$$

where σ'_v is the vertical effective stress and a is a coefficient which takes values in the range $a = 0.25 - 0.30$. Expressions have also been found for c_u in terms of the mean effective stress, σ'_m, which are also useful in applications

$$c_u = \bar{a}\sigma'_m. \tag{5.2}$$

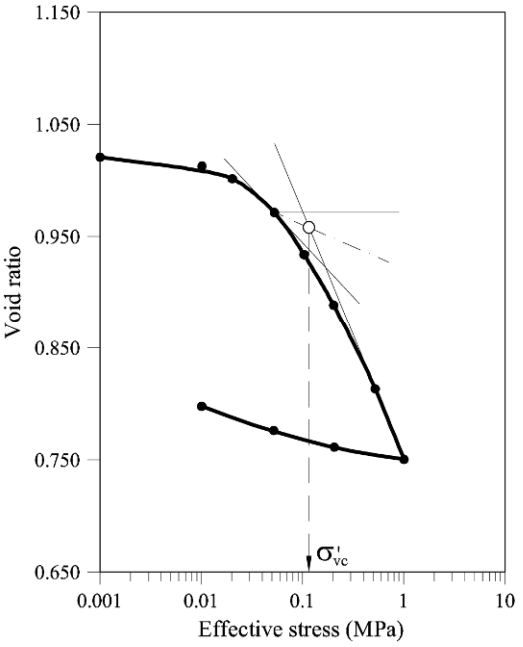

Figure 5.8 Oedometer test on a sample recovered at a depth of 12.50 m below the soil surface.

The expression for coefficient a and $\bar{a}$ can be derived following a theoretical procedure. For instance, Wood (1990) and Potts and Zdravkovic (1999) presented such derivations for a Cam Clay elastoplastic model (see Chapter 6). If the coefficient of earth pressure at rest, K_0, is known, the mean effective stress is given by

$$\sigma'_m = \frac{1+2K_0}{3}\sigma'_v \tag{5.3}$$

and, therefore,

$$\overline{a} = \frac{3a}{1+2K_0}. \tag{5.4}$$

For a normally consolidated clay, K_0 = 0.5, and $\overline{a} = 0.38$ if $a = 0.25$. This value for $\overline{a}$ will be used later. Further discussion on undrained strength is given in Chapter 6.

Simple shear tests performed in specimens recovered in the same deltaic formation of silty soils provided c_u/σ'_v values in the range 0.25 – 0.30. It appears that Equations (5.1) or (5.2) provide a good estimation of undrained strength in our case. It indicates that strength increases linearly with depth. The excavation of upper sands leaves the soil overconsolidated (provided that enough time has elapsed to dissipate pore pressures) but the undrained strength remains slightly below its original value because water content changes during unloading will remain small and the soil void ratio will essentially remain unchanged.

It follows that the first sinking of the caisson found a silty soil on the upper boundary of the silty clay deposit (at 9 m of depth with respect to the original ground level) having a value of c_u of around

$$c_u \approx 0.25\sigma'_v = 0.25 \cdot \gamma_{sub} \cdot \text{depth} = 0.25 \times 9 \text{ kN/m}^3 \times 9 \text{ m} = 20.25 \text{ kPa}, \tag{5.5}$$

where γ_{sub} is the average submerged unit weight for sands and silts that correspond to an average saturated unit weight (γ_{sat}) of 19 kN/m^3 and a water unit weight of 10 kN/m^3. On the lower contact between the silty layer and the dense sand level on the bottom (at a depth of 30 m), the undrained strength is

$$c_u = 0.25 \times 9 \text{ kN/m}^3 \times 30 \text{ m} = 67.5 \text{ kPa}. \tag{5.6}$$

The distribution of c_u with depth is plotted in Figure 5.6.

The remaining properties indicated in Figure 5.7 complete the description of the soil. Drained direct shear tests provided friction angles of 25º – 31º and negligible cohesion intercepts.

Additional data was provided by a cone penetration test (CPT) performed in the caisson foundation area during the design stage. The test was run at a water depth of 24 m on the sea side of the breakwater position. The record is shown in Figure 5.9. The test was run in several stages from the bottom of an advancing borehole. The initial penetration resistances at every repeated pushing operation are affected by a stress release induced by the boring excavation and possibly by some soil remoulding. If these initial parts of the penetration records are disregarded, the test shows a linear increase of the cone penetration resistance with depth, which is an indication of a normally consolidated state of the soil. Being at a water depth of 24 m the cone is recording the strength of silty clays (the upper sand layer is not present at these water depths). The undrained strength is correlated with point resistance, q_c, through (Lunne *et al*., 1997)

$$c_u = \frac{q_c - \sigma_v}{N_k}, \tag{5.7}$$

where σ_v is the total vertical stress at the current location and N_k is a "bearing capacity" factor, which takes values in the range $10-20$. For the Barcelona harbour soils, a value $N_k = 15$ provides c_u values consistent with undrained simple shear data. The CPT test in Figure 5.9 is a good indication of the normally consolidated conditions of the silt layer and, also, on the validity of Equation (5.1) with $a = 0.25$. The peak resistance values indicated in Figure 5.9 correspond to more resistant and dilatant sand layers. The silty clay strength corresponds to the minimum envelope of the q_c record, leaving aside the peaks and the disturbed initial parts of successive records.

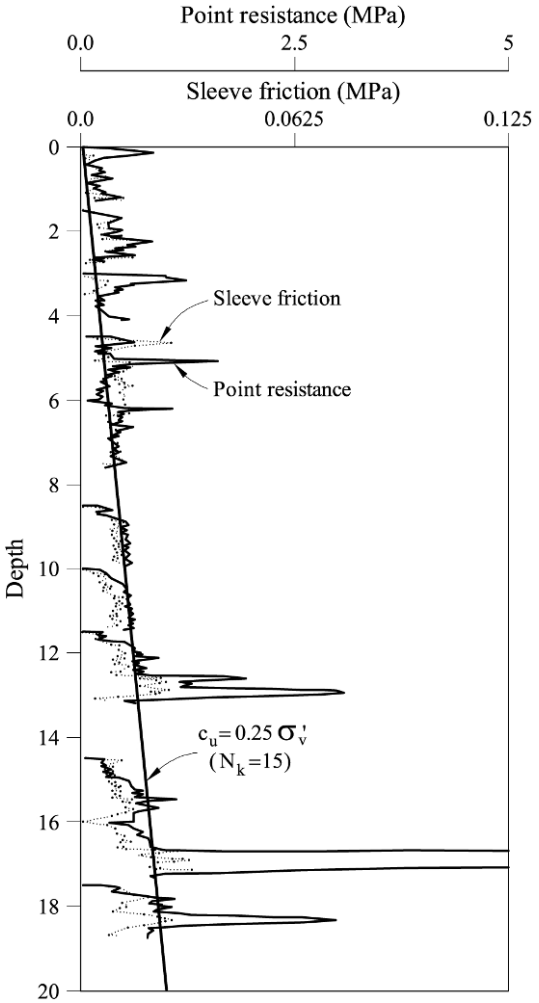

Figure 5.9 Cone penetration resistance and sleeve ratio of CPT test on foundation soils.

5.3.1 Liquefaction

The susceptibility to liquefaction of the low plasticity silty soil of the caisson foundation may be evaluated by performing undrained cyclic shear tests. But there is also a possibility of profiting the accumulated experience in earthquake engineering. A survey on the relationship between risk of liquefaction (under earthquake conditions) and type of soil (identified by its plasticity) is given in Figure 5.10 (Seed *et al*., 2003). The position of samples represented in Figure 5.7 is also indicated in the plasticity chart. They fall in the area of "potentially liquefiable" materials.

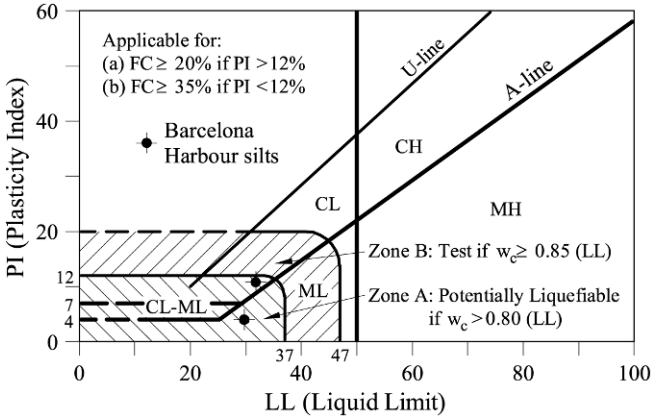

Figure 5.10 Criteria to assess the possibility of liquefaction of fine soils (Seed *et al*., 2003. With permission from ASCE). Also indicated are two representative plasticity points of Barcelona harbour silts.

Additional necessary information is to know the cyclic stress intensity leading to liquefaction. Different approaches may be found to estimate this stress level. In general, all of them try to estimate the stress ratio (τ/σ'_v: shear stress/vertical effective stress) inducing liquefaction.

Liquefaction is understood as a substantial reduction in undrained strength induced by the accumulation of positive pore water pressures during repeated undrained loading. At the limit, strength reduces to nil values but the back analysis of real cases indicates that some residual shear strength is generally available (Olson and Stark, 2002).

Figure 5.11 shows data originated in earthquake-induced liquefaction cases. It provides the critical stress ratio able to induce liquefaction as a function of the corrected SPT value. It corresponds to an earthquake magnitude of 7.5 and it refers to a reference confining stress of 0.65 atm (65 kPa). In an earthquake of magnitude 7.5, a few strong cycles are applied (15 – 20). This is significantly less than the number of waves hitting the breakwater at maximum storm intensity (H_s = 4 m). But despite the differences between earthquakes and wave loading on vertical caissons, it provides a useful reference value for τ/σ'_v: it may vary

between 0.05 and 0.1 if fines content FC < 5% for the range of SPT values (4 – 14) given in Figure 5.7. If FC increases (FC > 35%), the stress ratio increases to 0.1 – 0.2. Cyclic shear tests were performed (reported below) to determine more precisely the stress ratio for liquefaction.

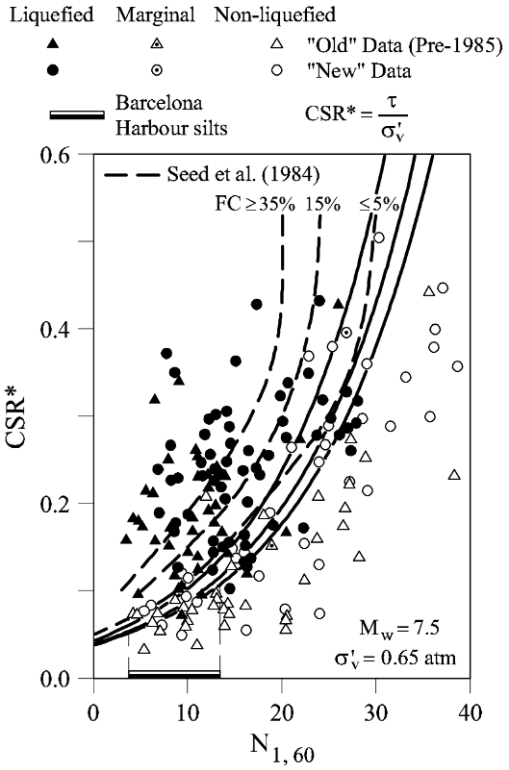

Figure 5.11 Critical stress ratio for liquefaction in terms of SPT values and fine's content (Seed *et al*., 2003. With permission from ASCE). Also indicated is the range of N_{SPT} values recorded in the soil investigation.

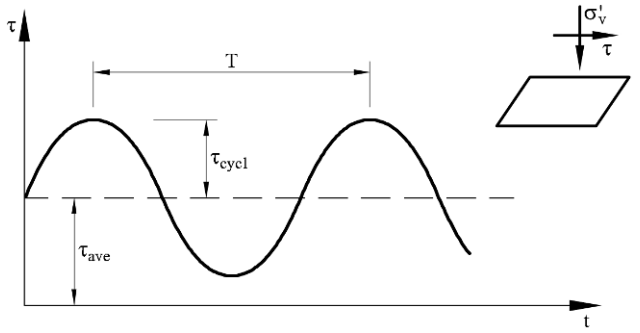

Figure 5.12 Definition of variables in cyclic shear loading.

A related experimental work was performed on undisturbed silt specimens, from the same geological formation, recovered in other Barcelona Harbour emplacements. Undrained simple shear cyclic tests were performed. The cyclic shear excitation is defined in Figure 5.12.

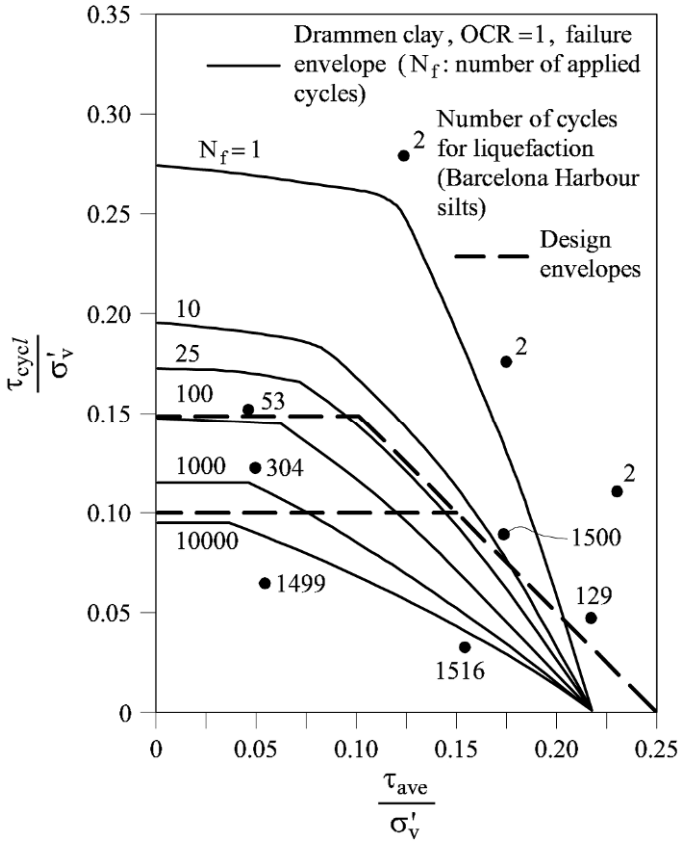

Figure 5.13 Results of cyclic undrained simple shear tests. Also indicated in the figure is data from Drammen clay (NGI 2002).

The periodic shear stress signal is described by an average value, τ_{ave}, a purely cyclic component, τ_{cycl} and a time period *T*. The results of tests performed are represented in a two-dimensional plot relating τ_{cycl}/σ'_v and τ_{ave}/σ'_v (Fig. 5.13). Each of the points in this plot indicates a combination of the pair (τ_{cycl}/σ'_v, τ_{ave}/σ'_v) which leads to failure of the specimen. The number associated with each point is the number of cycles applied. Increasing τ_{cycl}/σ'_v and/or τ_{ave}/σ'_v leads to a progressively smaller number of applied cycles necessary to induce failure. Failure is a consequence of the accumulation of pore pressures which result in increasing shear deformations because of the reduction in normal effective stress acting on the shearing plane. In practice, failure was accepted

when the shear strain reached 10%. Also indicated in the plot are the results for Norwegian Drammen clay for normally consolidated conditions.

The information given in the plot may be used to isolate a safe region for a given number of stress cycles applied. Safe regions are limited by the line

$$\frac{\tau_{cycl}}{\sigma'_v} + \frac{\tau_{ave}}{\sigma'_v} = \frac{c_u}{\sigma'_v} = a, \tag{5.8}$$

a being defined in Equation (5.1). Equation (5.8) tells that any combination of average and cyclic stress ratios leading to the static strength ratio will lead to failure. When the number of cycles increases, the safe region reduces in size because the cyclic stress ratio decreases. Two safe regions are shown in the plot in Figure 5.13 for a low and a high number of cycles (approximately 40 and 5,000), represented by the upper and lower dashed lines, respectively. In the first case, the limiting cyclic stress ratio is 0.15, provided the average stress ratio does not exceed 0.1. In the second case the limiting cyclic stress ratio is 0.1 for average stress ratios not exceeding 0.15. Beyond this average stress ratio, the cyclic component should be reduced. This plot will be used to estimate liquefaction conditions under wave action in the manner indicated below.

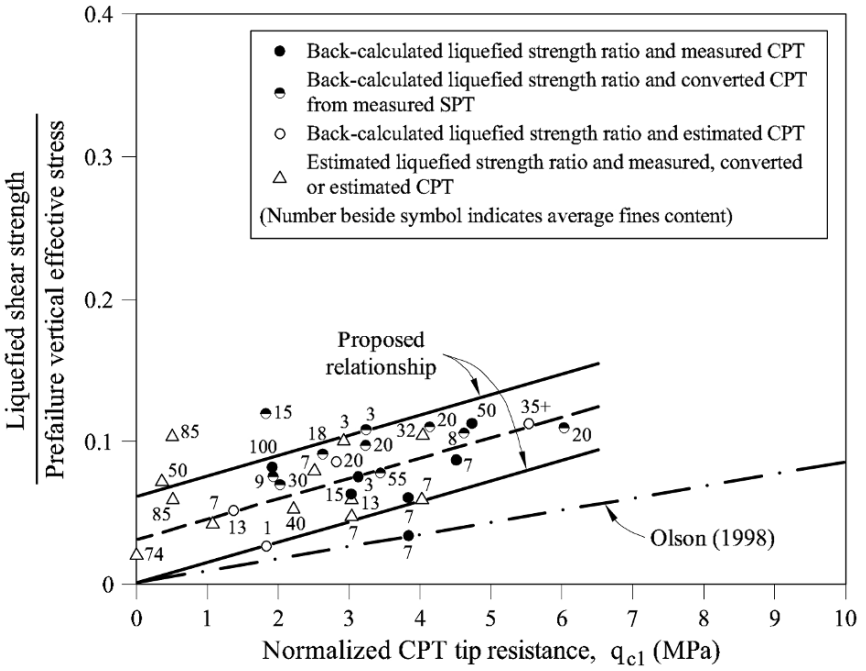

Figure 5.14 Liquefied strength ratio from liquefaction flow failure case histories (Olson and Stark, 2002 © 2008 NRC Canada. Reproduced with permission).

A final point concerns the static strength after liquefaction. In order to answer the question on the strength remaining after liquefaction, static undrained strength tests could be performed after cyclic loading leading to liquefaction. But it is also possible to back analyze some failures involving the flow of soil after cyclic loading. This information is necessary to analyze stability conditions once liquefaction is triggered. Figure 5.14 shows the correlation provided by Olson and Stark (2002) between the liquefied strength ratio and the normalized CPT point resistance. The q_c values reported above for the Barcelona Harbour silty soil, below the caisson foundation, are low (just a fraction of 1 MPa). Figure 5.14 shows that a low value of post-liquefaction strength ratio, ranging between 0 and 0.06, may be operative in this case.

5.4 Settlement Records and Their Interpretation

New caissons, built after the failure, were monitored and settlement records for an extended period of time were obtained (Fig. 5.15). They can be interpreted to derive average values of the foundation soil coefficient consolidation and stiffness. Note that the soil stiffness was already determined in oedometer tests performed on samples. However, the integrated field value provided by caisson settlement records is more reliable.

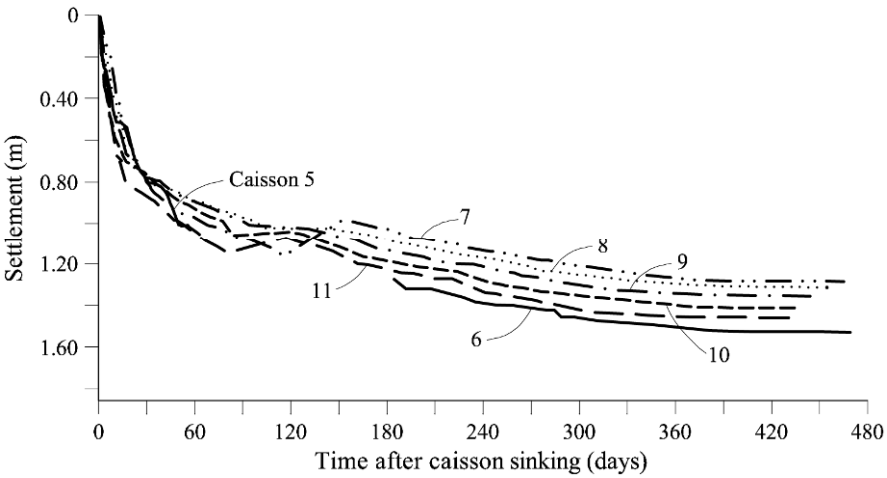

Figure 5.15 Settlement records for Caissons 5, 6, 7, 8, 9, 10 and 11 built after the failure of the first four caissons. Settlement records are plotted with a common time origin.

All the settlement records of caissons located in the vicinity of the failed ones were similar. They could be used to derive a field relationship between degree of consolidation, *U*, and time. *U* was calculated, for each time, as the ratio between the current settlement and the maximum value, at long term (around 600 days), which is easily identified in the settlement records. The relationship between *U* and time is plotted in Figure 5.16 in natural, log scale and square root of time. Settlements are linearly related to the logarithm of time with a good

approximation. The root of time plot is non-linear and this is an indication of the progressive reduction in time of the coefficient of consolidation, as shown below.

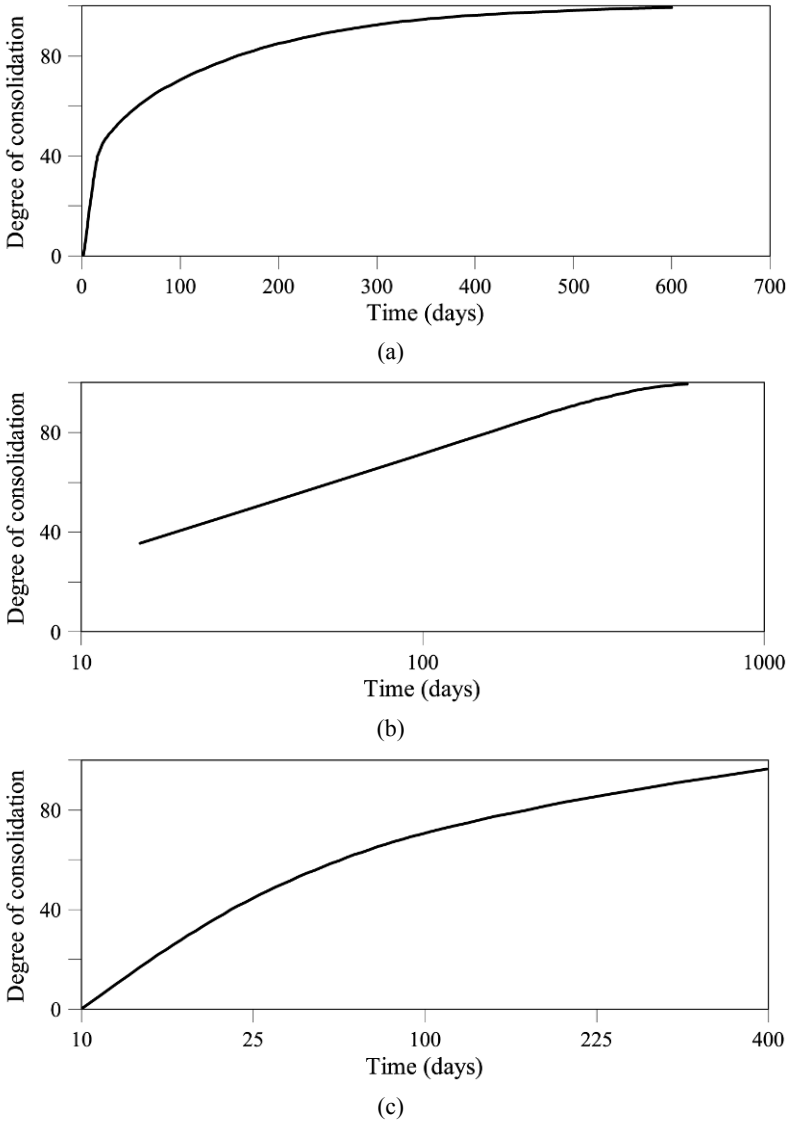

Figure 5.16 Average degree of consolidation from caisson settlement records: (a) natural time scale; (b) logarithmic time scale; (c) square root of time scale.

Davis and Poulos (1972) published the solution for the consolidation of a strip loading, which is useful to interpret the settlements of a caisson. They made assumptions equivalent to the classical one-dimensional Terzaghi consolidation

equation (constant coefficient of compressibility and permeability, soil deforms only in vertical direction). The solution for a permeable top and base is reproduced in Figure 5.17. For a given time, the degree of consolidation increases the more "three-dimensional" is the dissipation effect, i.e. for increasing values of the ratio: thickness of consolidation layer, h, over half width of the strip loading, b.

In our case, $h/b \approx 2$ and Figure 5.16 indicates that the solution is very close to the one-dimensional Terzaghi solution. The one-dimensional solution is almost exactly reproduced by the closed form equation

$$U = \sqrt{\frac{4T}{\pi}} \tag{5.9}$$

for $U < 0.526$ (see also Chapter 2). Since $T = c_v t / H^2$, Equation (5.9) may be used to find values of c_v (H is the half thickness of the consolidation layer: H = 10.5 m). For every pair of (U, t) values, an estimation of c_v is found. Table 5.1 provides c_v values for the first three months of the consolidation process.

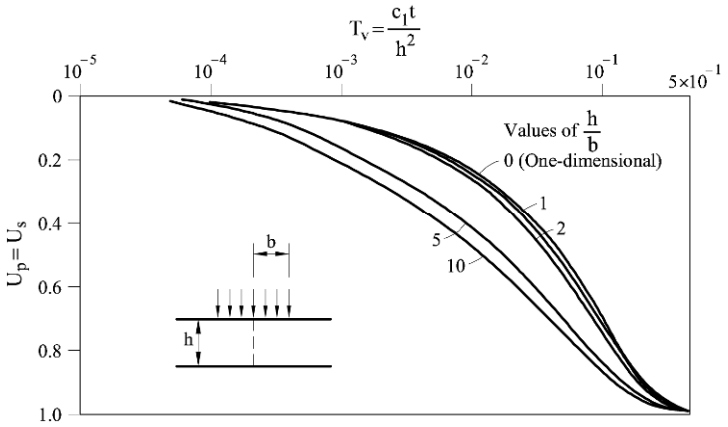

Figure 5.17 Degree of consolidation vs time factor. Strip footing, permeable top, permeable base (after Davis and Poulos, 1972; the original notation has been maintained).

Table 5.1 Coefficient of consolidation from time-settlement records.

t (days)	15	30	45	60	90
c_v (m^2/day)	0.748	0.702	0.60	0.53	0.46
c_v (cm^2/s)	0.086	0.081	0.07	0.061	0.053

As expected, c_v decreases with time probably because of the reduction in permeability as the soil void ratio decreases. In order to estimate the soil permeability, it is necessary to know the soil confined (elastic) stiffness, E_m, since

$$c_v = \frac{kE_m}{\gamma_w}. \tag{5.10}$$

E_m is expressed in terms of the compressibility index C_c as

$$E_m = \frac{(1+e_0)\sigma'_v}{0.434 C_c}. \tag{5.11}$$

Below the caisson base, at a depth equal to caisson half-width, the vertical stress in the soil is estimated to be $(22+10\times 8) = 300$ kPa. Therefore $E_m \approx 5{,}250$ kPa. Then, Equation (5.10) provides a soil permeability of $k = 1.5\times 10^{-8}$ m/s for $c_v = 0.7$ m^2/day. For the first stages of consolidation, which are the relevant ones in our case, the foundation soil reacts with a c_v value in the vicinity of 0.75 m^2/day.

The result, even if it is only approximate, indicates that the foundation soil is rather impervious. It will react in an undrained manner when subjected to relatively rapid loading (wave action or caisson sinking) and failure will be also undrained. The relevant strength property will be the undrained strength. Undrained failure will be also the critical one because these soft soils generate positive pore water pressures when sheared, which implies lower strengths, if compared with the drained case (see Fig. 5.18). Given an initial stress state I on the K_0 line, the undrained path (U) will lead to the shear strength c_u. By contrast, a direct application of Coulomb's law implies path D and a higher, unrealistic, and unsafe shear strength τ_f. See Chapter 6 for a more detailed discussion on this issue.

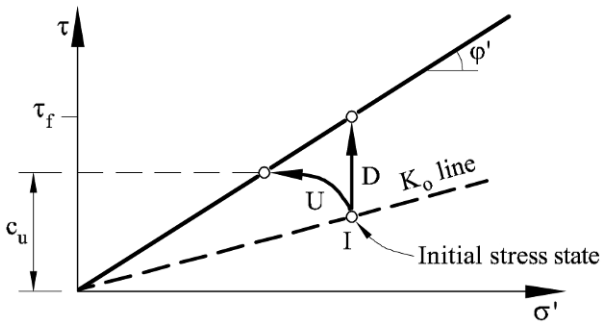

Figure 5.18. Undrained and drained triaxial stress paths.

5.5 Safety During Caisson Sinking

5.5.1 Caisson weight

Once dredging ended in October 2000, the coarse granular base was backfilled into the opened trench on the sea bottom. The berm was levelled and prepared for caisson sinking in May 2001. Actual sinking took place in the middle of October 2001. The storm and the caisson failure arrived 20 days later. (The caisson construction history is schematically indicated in Fig. 5.19.)

Unloading due to dredging and the subsequent granular filling did not restore exactly the initial effective stress in the clayey silt but it was very close. Changes in water content were minor and therefore the natural soil essentially maintained the original undrained strength profile shown in Figure 5.6.

Caissons cell volume amounts to 55% of total volume. When cells are filled with water, the caisson sinks. The granular base was levelled at elevation – 17.50 m and, therefore, after sinking, the upper 2 m of caissons remained above the sea level. The effective weight of the caisson per unit length (1 m) in the longitudinal direction is:

$$W'_{\text{water}} = 19.6 \times 19.5 \times \left(0.55\gamma_w + 0.45\gamma_c\right) - 19.6 \times 17.5\gamma_w \tag{5.12}$$

where γ_c, γ_w are the unit weights of concrete and sea water. For $\gamma_c = 23$ kN/m^3 and $\gamma_w = 10$ kN/m^3, $W'_{\text{water}} = 2,628$ kN/m. The vertical net stress against the foundation is $\sigma_v^{\text{water}} = 2,628$ kN/m/19.6 m = 134 kPa.

When filled with submerged sand the caisson effective weight against its foundation, per unit longitudinal length of caisson, is

$$W'_{\text{sand}} = 19.6 \times 19.5 \times \left(0.55\gamma_{\text{sand}} + 0.45\gamma_c\right) - 19.6 \times 17.5\gamma_w \tag{5.13}$$

It was estimated that γ_{sand} = 18 kN/m^3. Also, γ_{concrete} = 23 kN/m^3 and therefore W'_{sand} = Q = 4,310 kN/m. The applied effective vertical stress on the caisson base is q = Q/19.6 m = 220 kPa.

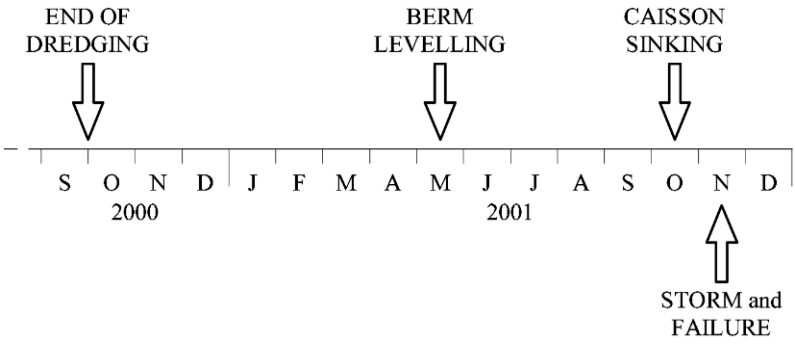

Figure 5.19 History of caisson construction and failure.

5.5.2 Bearing capacity

Davis and Booker (1973) found the exact solution for the bearing capacity of a strip footing when the undrained strength increases linearly with depth according to the relationship

$$c_u = c_{u0} + \rho z, \tag{5.14}$$

where ρ is a constant. The upper granular layer (Fig. 5.6) introduces some additional bearing capacity, but it is probably very small. In fact, the lateral extent of the berm is small. If a simple failure mechanism is considered, the sole effect of the granular layer is to provide a frictional resistance T (Fig. 5.20). Being at the surface and having only a thickness of around 2 m, the confining stress in the

granular berm is very small compared with the contribution of the natural soil. It will be accepted, for simplicity, that only the natural soil contributed to the bearing capacity.

The theoretical bearing capacity was written, by Davis and Booker (1973),

$$Q/B = F\left[(\pi + 2)c_{u0} + \rho b/4\right], \tag{5.15}$$

where F is a correction factor that depends on the ratio $\rho b/c_{u0}$ and may be found in Figure 5.21.

Equation (5.15), for c_{u0} = 20.25 kPa; $\rho = (67.5 - 20.25)\,\text{kPa}/21\,\text{m} = 2.25\,\text{kN/m}^3$ and F = 1.35 (for $\rho b/c_{u0} = 2.25\,\text{kN/m}^3 \times 19.6\,\text{m}/20.25\,\text{kN/m}^2 = 2.2$; see Figure 5.20 for rough footing), provides $Q/b = 155$ kPa, which is lower than the applied caisson net stress if filled with sand (220 kPa).

Caissons, however, were initially filled with water before replacing it with sand. The net stress on the foundation of a water filled caisson is 134 kPa. Therefore, the safety factor when the caissons were sunk with water ballast can be calculated as $SF = 155/134 = 1.16$.

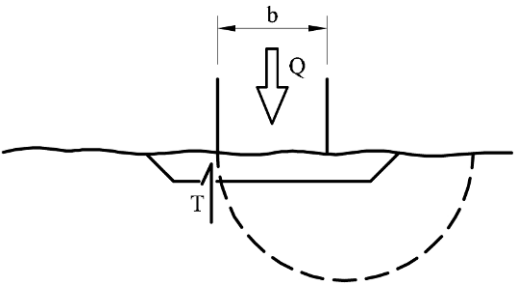

Figure 5.20 Sketch to illustrate the frictional resistance to failure offered by the granular berm.

The theoretical expression (5.15) predicts conditions very close to failure at the time of caisson sinking. Three-dimensional effects, due to the finite rectangular shape of the caissons base, leads to an increase of the bearing capacity and this effect may explain that the caissons remained stable. Also, the limited thickness of the upper granular term provided some additional bearing capacity. On the other hand, if the undrained strength was actually somewhat higher (Eq. (5.1) with a = 0.30, for instance), the safety factor against failure would also increase. Safety factor increases linearly with c_u, and a value of a = 0.30 would result in $SF = 186/134 = 1.4$.

It is difficult to be more precise, but the fact is that the caissons did not fail during sinking. However, the estimation made points towards a small safety factor above one. Beyond this moment, the consolidation of the soil under the caisson's weight will increase the available shear strength in the natural soil. The caisson was then loaded with its definite weight (when filled with saturated sand), it

consolidated during a few weeks, and eventually it received the storm-wave loading.

Before analyzing these processes, it is worth investigating if the theoretical undrained bearing capacity obtained by Davis and Booker for a strip footing on a clay soil whose strength increases with depth, may be approximated by a simpler kinematically admissible mechanism, using the upper bound theorem of plasticity. The reason behind this approach is to prepare the ground for subsequent calculations involving the wave action and a more complex distribution of undrained strength with depth. In fact, the consolidation process will lead to a "map" of c_u values which will match the "map" of mean effective stresses (Eq. (5.2)). This distribution, changing with time, will be substantially different from a linear variation of c_u and it will not be amenable to theoretical solutions. However, the plasticity theorems still provide an approximation. It then seems wise to try to establish some confidence on the assumed failure mechanism (based on the upper bound theorem). The way to do it is by comparing the exact solution provided by Davis and Booker (1973) with the upper bound approximation.

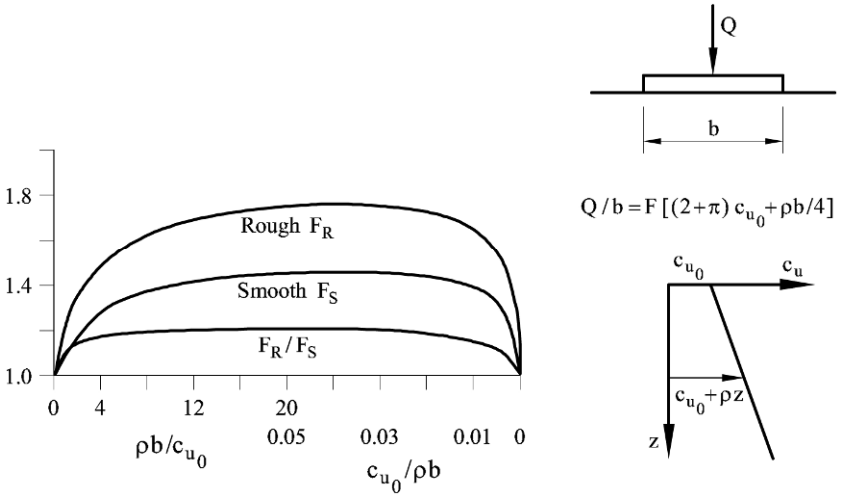

Figure 5.21 Correction factors for rough and smooth footings (after Davis and Booker, 1973).

5.5.3 An upper bound solution for a rough strip footing founded on clay with a linearly increasing strength with depth

Figure 5.22 shows the critical velocity field found by Davis and Booker (1973) in their exact solution to the bearing capacity problem (infinite, rigid smooth footing). The mechanism is symmetric with respect to the axis of the footing.

Even if the rough footing is a more realistic case, this mechanism suggests the simplified symmetric mechanism, based on rigid triangular wedges, indicated in Figure 5.23.

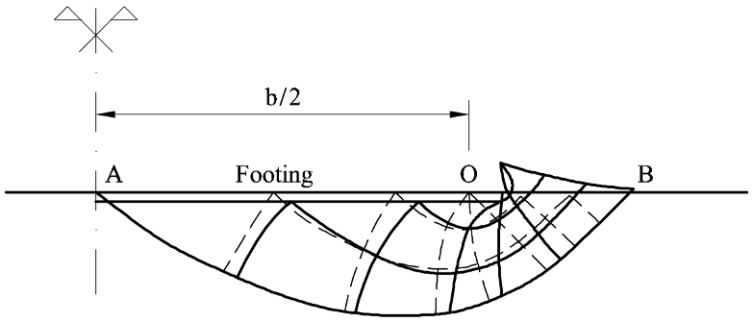

Figure 5.22 Velocity field for smooth footing (after Davis and Booker, 1973).

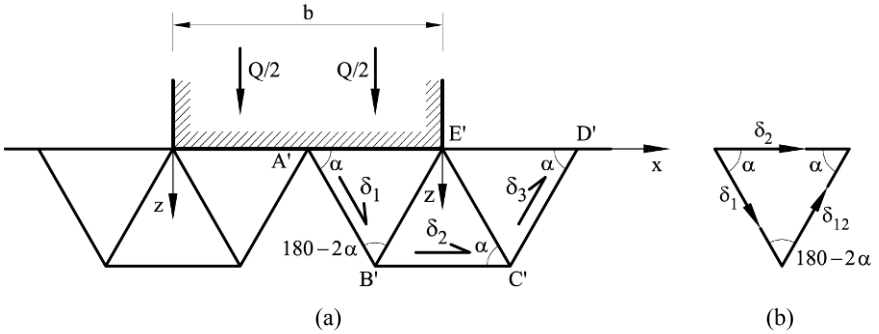

Figure 5.23 Symmetric failure mechanism for upper bound analysis of strip footing under vertical load.

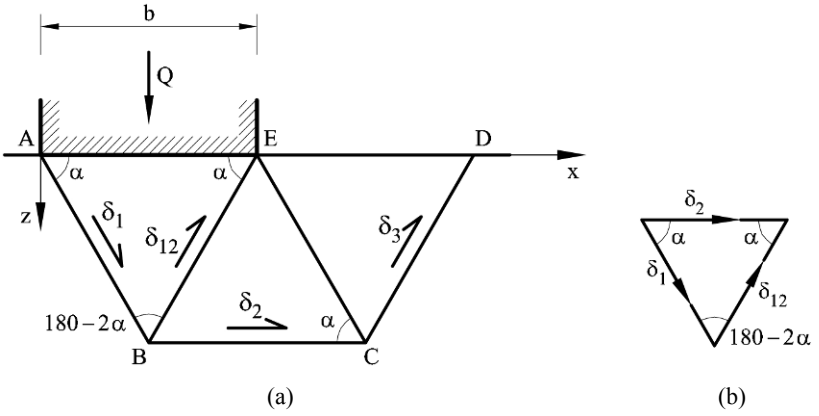

Figure 5.24 Nonsymmetric failure mechanism for upper bound analysis of strip footing under vertical load.

Consider one of the two symmetric mechanisms that receive half of the external load ($Q/2$). This mechanism will be optimized with respect to the angle α

shown in Figure 5.23. The motion of this mechanism is characterized by the virtual displacement rate vector δ_1, which defines the motion of wedge A′B′E′ sliding on the straight segment A′B′. The length of segment A′B′ in terms of caisson width, *b*, is $L = b/(4\cos\alpha)$. The undrained strength will be defined by the linear function $c_u(z) = c_{u0} + \rho z$.

The dissipation along A′B′ is calculated as follows

$$W_{A'B'} = \int_{A'}^{B'} c_u(z)\delta_1 \mathrm{d}l = \int_{A'}^{B'} (c_{u0} + \rho z)\delta_1 \mathrm{d}l = \int_{A'}^{B'} (c_{u0} + \rho l \sin\alpha)\delta_1 \mathrm{d}l = \\ = \delta_1 \left[c_{u0} l + \frac{\rho}{2} l^2 \sin\alpha \right]_0^L = \delta_1 \frac{b}{4\cos\alpha} \left(c_{u0} + \frac{\rho b}{8} \tan\alpha \right). \tag{5.16}$$

Consider now the dissipation along B′C′. The relative motion δ_2 between the moving wedges B′C′E′ and the rigid soil along B′C′ is given by $\delta_2 = 2\delta_1 \cos\alpha$ in view of the motion compatibility condition expressed in Figure 5.23b.

The *z* coordinate of line B′C′ is $z = b\tan\alpha/4$; then

$$W_{B'C'} = c_u \left(z = \frac{b\tan\alpha}{4} \right) \delta_2 \frac{b}{2} = \left(c_{u0} b\cos\alpha + \rho \frac{b^2}{4} \sin\alpha \right) \delta_1. \tag{5.17}$$

Considering the hypothesis of rough footing, dissipation along the line A′E′ is

$$W_{A'E'} = c_{u0} \frac{b}{2} \delta_1 \cos\alpha. \tag{5.18}$$

Dissipation along lines A′B′, B′E′, E′C′ and C′D′ is equal and therefore the total internal dissipation work on the mechanism will be

$$W_{\text{int}} = 4W_{A'B'} + W_{B'C'} + W_{A'E'}. \tag{5.19}$$

The external work performed by *Q*/2 is calculated as

$$W_{\text{ext}} = \frac{Q}{2} \delta_1 \sin\alpha. \tag{5.20}$$

Making $W_{\text{int}} = W_{\text{ext}}$, *Q* is isolated in terms of α, c_{u0}, ρ, *b*:

$$Q = \frac{b}{4} \frac{\left(8c_{u0} + \rho b \tan\alpha + 12c_{u0}\cos^2\alpha + 2\rho b \sin\alpha\cos\alpha\right)}{\sin\alpha\cos\alpha}. \tag{5.21}$$

The best upper bound solution for *Q* is its minimum value with respect to α. This minimization calculation was performed with the help of the built in "solve" function including in Excel. For *b* = 19.6 m, c_{u0} = 20.25 kPa, and ρ = 2.25 kN/m^3 a minimum value of *Q*/*b* = 182 kPa is obtained for a critical angle α equal to 50.8º.

The theoretical value (Davis and Booker, 1973) for rough footing provides a

value Q/b = 155 kPa. The error of the simple upper bound mechanism is 17%, a reasonable value in practical terms. This result indicates that the triangular wedge mechanism in Figure 5.22 is an acceptable approximation to calculate the bearing capacity factor for strip footings resting on a clay soil with a linearly increasing strength with depth. It should be stressed that the main purpose of the analysis developed in the remaining part of the chapter is to examine the variation of safety factor during the consolidation after caisson sinking, subsequent filling with sand, and storm action. The upper bound calculations provide a simple and practical tool to evaluate the sequence of events leading to caisson failure.

However, if a horizontal load is also acting on the caisson, because of wave action, a symmetric mechanism cannot possibly occur and a more likely mechanism is indicated in Figure 5.24. We call it a nonsymmetric failure mechanism. Let us consider first this mechanism under a vertical load. The calculation is now almost identical to the previous one. Note that in this case the caisson will not displace with respect to the wedge AEB along the line AE. Therefore, no dissipation will be calculated on segment AE. Repeating previous steps, the dissipation on segments AE and BC will be

$$W_{\mathrm{AB}} = \frac{\delta_1 b}{2\cos\alpha}\left(c_{u0} + \frac{1}{4}\rho b \tan\alpha\right), \tag{5.22}$$

$$W_{\mathrm{BC}} = \left(2bc_{u0}\cos\alpha + \rho b^2 \sin\alpha\right)\delta_1. \tag{5.23}$$

The internal dissipation work will be $W_{\mathrm{int}} = 4W_{AB} + W_{BC}$. The external work is now given by:

$$W_{\mathrm{ext}} = Q\delta_1 \sin\alpha. \tag{5.24}$$

Making the two works equal and isolating Q,

$$Q = \frac{b}{2}\frac{\left(4c_{u0} + \rho b \tan\alpha + 4c_{u0}\cos^2\alpha + 2\rho b \sin\alpha\cos\alpha\right)}{\sin\alpha\cos\alpha}, \tag{5.25}$$

which is different from the Q value calculated for the symmetric mechanism.

The minimization of Q with respect to α was also performed on an Excel sheet. For the same parameters previously considered (b = 19.6 m; c_{u0} = 20.25 kPa; ρ = 2.25 kN/m^3), a failure unit load Q/b = 209 kPa was calculated (for a critical angle α equal to 44.5º) which is 15% higher than the load calculated for the symmetric mechanism. This nonsymmetric mechanism will be used when wave action is considered, as mentioned above.

Caisson consolidation resulted in increasing c_u values and in increasing safety factor against bearing capacity failure.

Two weeks after the caisson first sinking, caisson cells were filled with sand. This increase in net weight will be also analyzed below in order to determine the associated safety factor. In the days that followed the sand filling, caisson consolidation continued and the soil undrained strength had to be estimated before

analyzing the storm effect on caissons.

Therefore, the next step in the analysis was to investigate the caisson consolidation and the increase in soil strength.

5.6 Caisson Consolidation. Increase in Soil Strength

Actual settlement records of caissons built after the failure, shown in Figure 5.15, indicate that a significant consolidation may be achieved in a few weeks. Points of the soft foundation soil close to the upper pervious granular layer would experience a rapid consolidation under the full caisson loading. Clay levels located close to the lower pervious sandy boundary will also consolidate fast but the stress increments reaching the lower sand levels will be significantly lower. Caisson consolidation leads to a progressive increase in effective stress and therefore to an increase in undrained strength. For the reasons mentioned, however, the new distribution of undrained strength values will be non-homogeneous and also far from the initial linear distribution with depth. This will be especially the case of the foundation soil directly under the caissons.

The increments of undrained strength will be simply calculated as a fraction of the increment in effective mean stress through Equation (5.2). Therefore, the objective now is to calculate the distribution of effective mean stress under the caisson loading, taking into account the consolidation process. The calculation will be split into two parts:

- Stress increments under a strip footing and determination of excess pore pressures.
- Dissipation of the induced excess pore pressures.

5.6.1 Stress increments under a strip footing and determination of excess pore pressures

This analysis will be guided by the subsequent use of the calculated undrained strengths. In fact, the ultimate objective is to determine the failure load and to compare it with the actual caisson loading. Failure conditions will be calculated by means of the upper bound theorem of plasticity, through the mechanisms already examined (Figs. 5.23 and 5.24). Consider in Figure 5.25 the two alternative mechanisms proposed here: a symmetric one (already identified as an adequate solution for vertical loading only) and the non-symmetric, one which will be employed when including wave action.

Upper bound calculation will require the determination of plastic work dissipation on segments AB, A′B′, etc. Since non-linear strength variations will be the rule, a minimum of three control points are proposed to estimate by a simple numerical integration, the average strength on each of the sliding surfaces of the two mechanisms shown in the figure. Those points (marked as open circles) define a number of vertical profiles characterized by the horizontal coordinate distances to the left caisson foundation corner indicated in Figure 5.25.

Pore pressure dissipation will be dominated by the vertical flow towards the upper and lower drained boundaries. A hypothesis of vertical consolidation, which is close to real conditions, as justified in Equation (5.4), helps to perform the

consolidation analysis. The following sequence of steps will be considered (the starting point – time = 0 – will be the initial sinking of caissons):

a) Stress increments in the foundations are determined. Elastic solutions for strip loading are used. Stress calculations are performed in vertical profiles located on the horizontal coordinates shown in Figure 5.25 (x = 0, 4.9, 9.8 m… etc.). The reason for this choice has already been given.
b) Mean total stress will be computed in points located on the vertical profiles. Excess pore pressures (over hydrostatic values) will be made equal to the increments of mean stress. This is a reasonable and sufficiently accurate assumption.
c) Excess pore pressures will be dissipated vertically towards the upper and lower drainage boundaries in a one-dimensional process. A time period of 14 days will provide the state of the foundation before sand filling the caissons.
d) Mean effective stress will be calculated as a difference between calculated total stresses and pore water pressures. An updated distribution of c_u values will be calculated through Equation (5.2).
e) Caisson failure loads will be determined through the upper bound theorem. The safety factor will be determined.

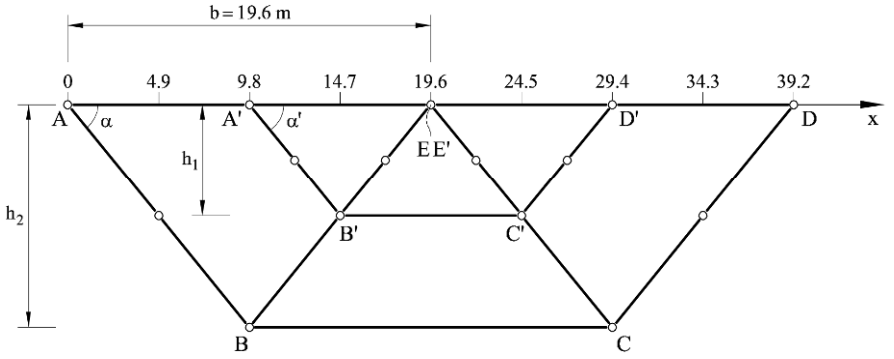

Figure 5.25 Geometry of the symmetric (A′B′C′D′E′) and nonsymmetric (ABCDE) failure mechanisms. Position of vertical profiles for the calculation of undrained soil strength.

5.6.2 Stress increments

a) Calculation of stress increments in the foundation

Poulos and Davis (1973) published the stress distribution beneath a strip loading uniformly loaded. With reference to Figure 5.26, the stresses on a point in an elastic half space, defined by their coordinates (x,z) or, alternatively, by angles α and δ are given by

$$\sigma_z = \frac{q}{\pi}\left[\alpha + \sin\alpha\cos(\alpha + 2\delta)\right], \tag{5.26a}$$

$$\sigma_x = \frac{q}{\pi}\left[\alpha - \sin\alpha\cos(\alpha + 2\delta)\right], \tag{5.26b}$$

$$\sigma_y = \nu(\sigma_x + \sigma_z), \tag{5.26c}$$

$$\tau_{xz} = \frac{q}{\pi}\sin\alpha\cos(\alpha + 2\delta). \tag{5.26d}$$

b) Mean stress and initial excess pore pressures

The mean stress is calculated as

$$\sigma_m = p = \frac{\sigma_x + \sigma_y + \sigma_z}{3} = \frac{2(1+\nu)}{3}\frac{q}{\pi}\alpha, \tag{5.27}$$

where

$$\alpha = \arctan\left(\frac{x}{z}\right) + \arctan\left(\frac{b-x}{z}\right) \tag{5.28}$$

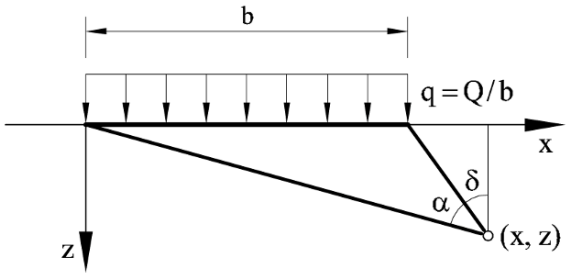

Figure 5.26 Uniform strip loading. Coordinate system (Poulos and Davis, 1973).

5.6.3 Initial excess pore pressures

The calculated profiles of σ_m (which is equal to the initial excess pore pressure) at a few horizontal coordinates indicated in Figure 5.25 (x = 9.8, 12.25, 19.6, 22.05 26.95 and 34.30 m) are given in Figure 5.28 for t = 0. The actual sequence of caisson loading is shown in Figure 5.27. After sinking, caissons remained full of water during 14 days. The external load q in this period was the net stress applied by the caisson at the time of sinking (caissons filled with water: $q = Q/b$ = 134 kPa). The time of sinking is t = 0 for the remaining of the analysis. At t = 14 days caisson cells were filled with sand and the net stress on foundation increased to 220 kPa. The storm arrived at t = 21 days.

Figure 5.28 shows two kinds of shapes for the distribution of the initial excess pore pressure due to the caisson loading (solid line). Under the caisson ($x = 0^+$ to

$x = 19.6$ m), the mean stress reaches a maximum at the caisson-soil contact and a minimum at the bottom of the clay stratum (at a depth of 21 m under the caisson's base, where the pervious sand layer is encountered). On both sides of the caisson ($x > 19.6$ m) the stress increment at the surface is zero. It increases to reach a maximum at some intermediate depth and decreases again. The intensity of the mean stress increments decreases as the distance to the caisson base increases.

A dissipation process of excess pore pressures will immediately start towards the upper and lower drainage boundaries and, in parallel, mean effective stresses will increase. These are steps c) and d) of the description of the process leading to an increase in soil strength.

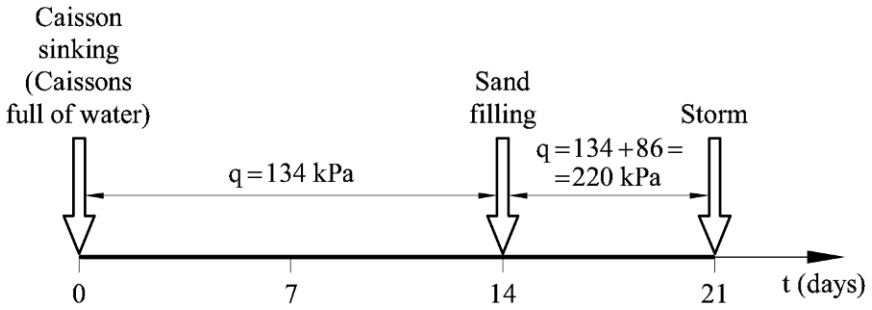

Figure 5.27 Caisson loading sequence.

5.6.4 Excess pore pressure dissipation

The initial excess pore pressures plotted in Figure 5.28 do not follow simple linear laws. This prevents the direct use of consolidation solutions given in most soil mechanics textbooks. Probably the simplest curve fitting all the profiles shown in the figure to a reasonable approximation is a parabola:

$$f(z) = A + Bz + Cz^2, \tag{5.29}$$

where $f(z)$ is the initial excess pore pressure, which is a function of the vertical coordinate. *A, B, C* can be determined by curve fitting procedures or simply by selecting three points on the curve at different *z* to be fitted. Then, the coefficients *A*, *B*, *C* are derived from the following system of algebraic equations:

$$f(z_1) = A + Bz_1 + Cz_1^2, \tag{5.30a}$$

$$f(z_2) = A + Bz_2 + Cz_2^2, \tag{5.30b}$$

$$f(z_3) = A + Bz_3 + Cz_3^2. \tag{5.30c}$$

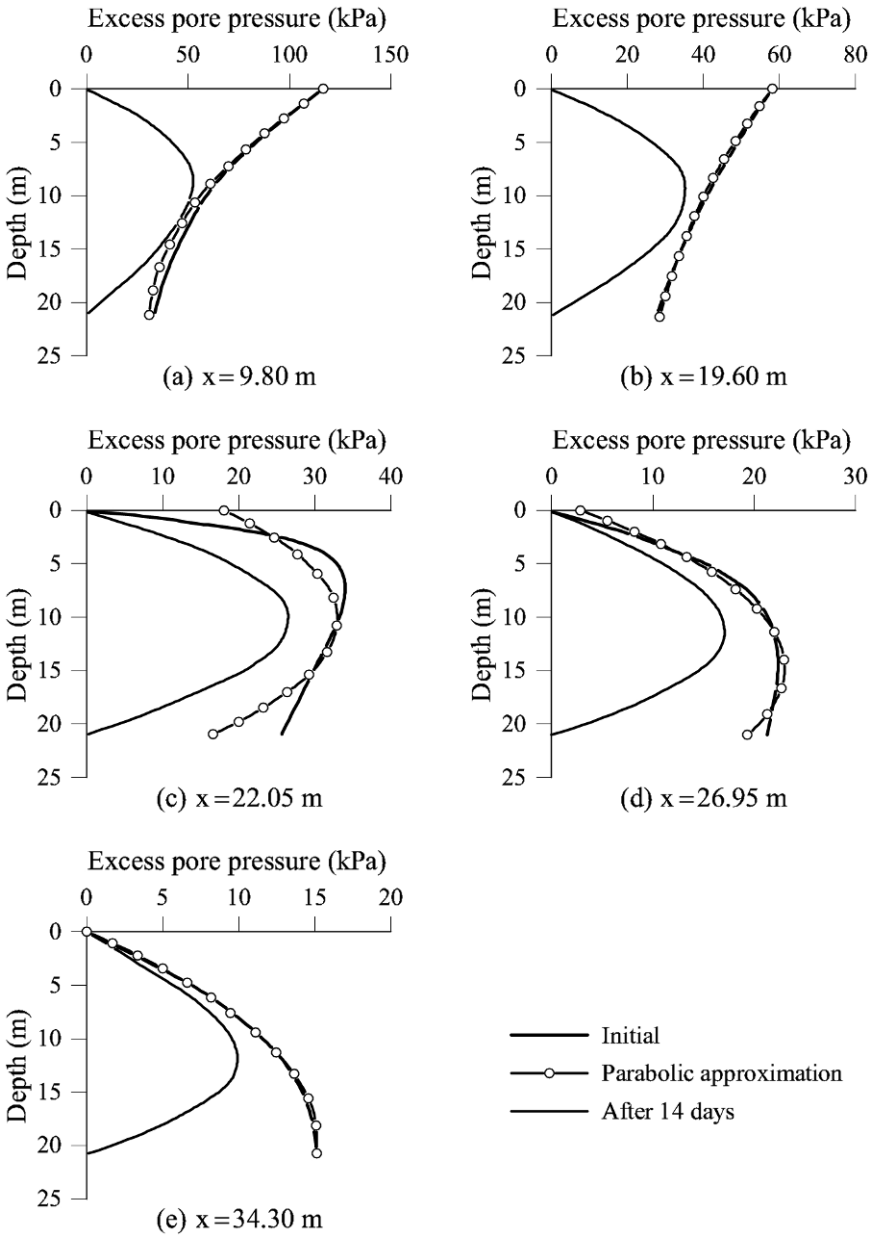

Figure 5.28 Excess pore pressures at the vertical profiles defined by x = 9.8, 19.6, 22.05, 26.95 and 34.30 m in Figure 5.25. Each one of the plots provides the calculated initial excess pore pressure, its parabolic approximation, and the excess pore pressure profile calculated after 14 days of consolidation.

The "solve" function of the Maple program provides the following solution:

$$A = \frac{f(z_1)\left[z_2^2 z_3 - z_2 z_3^2\right] + f(z_2)\left[z_1 z_3^2 - z_1^2 z_3\right] + f(z_3)\left[z_1^2 z_2 - z_1 z_2^2\right]}{z_2 z_1^2 + z_3 z_2^2 + z_1 z_3^2 - z_3 z_1^2 - z_1 z_2^2 - z_2 z_3^2}, \tag{5.31a}$$

$$B = -\frac{z_1^2\left[f(z_3) - f(z_2)\right] + z_2^2\left[f(z_1) - f(z_3)\right] + z_3^2\left[f(z_2) - f(z_1)\right]}{z_2 z_1^2 + z_3 z_2^2 + z_1 z_3^2 - z_3 z_1^2 - z_1 z_2^2 - z_2 z_3^2}, \tag{5.31b}$$

$$C = \frac{z_1\left[f(z_3) - f(z_2)\right] + z_2\left[f(z_1) - f(z_3)\right] + z_3\left[f(z_2) - f(z_1)\right]}{z_2 z_1^2 + z_3 z_2^2 + z_1 z_3^2 - z_3 z_1^2 - z_1 z_2^2 - z_2 z_3^2}. \tag{5.31c}$$

The preceding equations were introduced in an Excel sheet and the fit of the excess pore pressure profiles was obtained by selecting points of the theoretical distribution of Δu (=Δp). The selection of fitting points was directed towards a faithful representation of pore pressures in the central zone of the consolidating layer. The reason is that the excess pore pressures at the upper and lower boundaries will become zero (this is the boundary condition) immediately after the start of the consolidation process. In other words, the precise representation of the extreme values of excess pore pressures is not so relevant. Of course, the total area of the excess pore pressures should be maintained equivalent in the theoretical and the fitted initial pore pressure profile.

The result of this fitting process is also given in Figure 5.28. The parabolic fit is very good under the caisson and at a certain distance from it. The most difficult fit is for vertical profiles outside the caisson but in its immediate vicinity. However, increasing the degree of the polynomial approximation was probably not a reasonable decision in view of the associated complexity and the limited influence of an exact representation of initial excess pore pressures.

The excess pore pressures will be assumed to dissipate vertically, as mentioned before. The problem is schematically shown in Figure 5.29. The excess pore pressure $u(z,t)$ must satisfy Terzaghi's classical equation

$$c_v \frac{\partial^2 u}{\partial z^2} = \frac{\partial u}{\partial t}, \tag{5.32}$$

where c_v is the coefficient of consolidation subjected to the following boundary and initial conditions:

Boundary condition ($\forall t$):

$$u(z = 0, t) = 0, \tag{5.33a}$$

$$u(z = 2H = 21\ \text{m}, t) = 0. \tag{5.33b}$$

Initial condition ($\forall z$):

$$u(z, t=0) = A + Bz + Cz^2, \tag{5.34}$$

where coefficients A, B and C are determined through Equations (5.31a,b,c) for each of the vertical excess pore pressure profiles defined in Figure 5.25.

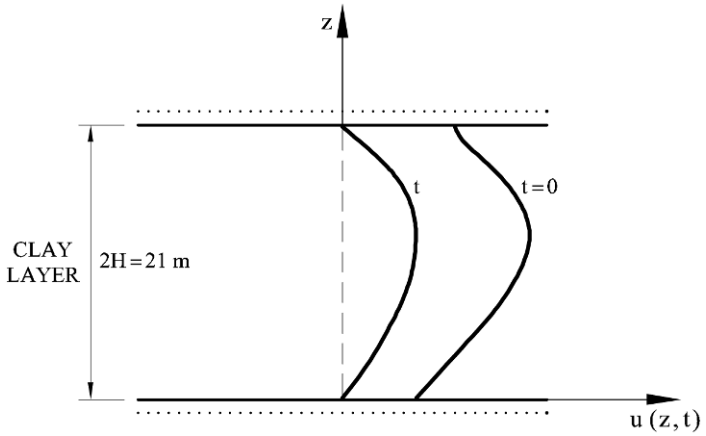

Figure 5.29 Double-drained consolidation induced by caisson sinking at t = 0 and excess pore pressures.

Note that the similarity of excess pore pressures under the caisson will lead to similar values of coefficients A, B, C. Therefore, no significant pore pressure gradients in the horizontal direction will occur under the central part of the caisson foundations. A one-dimensional vertical dissipation is close to real conditions. In the vicinity of the edges (compare pore pressure profiles for x = 19.6 m and x = 22.95 m in Fig. 5.28), horizontal pore pressures gradients are higher, however. This will lead to some horizontal flow components which are not taken into account. At increasing distance from the caisson (pore pressure profiles at x = 26.95, 34.30 m in Fig. 5.28) they again become similar among them and the vertical dissipation dominates the process. Recall also that the solution of the two-dimensional consolidation problem (in terms of the degree of consolidation) was very close to the one-dimensional case for the geometry of the caisson and its foundation (Fig. 5.17).

In terms of the dimensionless variables $Z = z/H$; $T = t/\tau$ and $W = u/u_0$, where τ and u_0 are a reference time $\left(\tau = H^2/c_v\right)$ and a reference pressure, the consolidation equation becomes

$$\frac{\partial^2 W}{\partial Z^2} = \frac{\partial W}{\partial T}. \tag{5.35}$$

The boundary and initial conditions become

Boundary condition ($\forall T$):

$$W\left(Z=0,T\right)=0, \tag{5.36a}$$

$$W\left(Z=2,T\right)=0. \tag{5.36b}$$

Initial condition ($\forall Z$):

$$W\left(Z,T=0\right)=A+BHZ+CH^2Z^2=\overline{A}+\overline{B}Z+\overline{C}Z^2, \tag{5.37}$$

where a new set of constants ($\overline{A}=A$, $\overline{B}=BH$ and $\overline{C}=CH^2$) are defined to describe the initial parabolic excess pore pressure in terms of the dimensionless coordinate *Z*.

The general solution of Equations (5.35), (5.36) and (5.37) is (Alonso and Krizek, 1975)

$$W\left(Z,T\right)=\int_R g\left(Z,T/Z_0,0\right)f\left(Z_0\right)\mathrm{d}Z_0-\int_0^T \mathrm{d}T_0\int_S \frac{\partial g\left(Z,T/Z_0,T_0\right)}{\partial n_0}W\left(Z_0,T_0\right)\mathrm{d}S_0, \tag{5.38}$$

where *R* is the domain of integration (*Z* = 0 to *Z* = 2 in our case); *S* is the boundary of *R* (*Z* = 0; *Z* = 2); n_0 is the normal to the boundary (the *Z* direction); $W(Z_0,T_0)$ are the boundary conditions (homogeneous in the present case), and *g* is the Green function associated with the consolidation equation.

Function $g\left(Z,T/Z_0,T_0\right)$ is the solution of the consolidation equation, in the case of homogeneous boundary conditions, when a unit "impulse" increase in pore pressure is introduced in coordinate $Z = Z_0$ at time $T = T_0$. The solution to this problem is

$$g\left(Z,T/Z_0,T_0\right)=\sum_{n=1}^{\infty}\sin\left(\frac{n\pi Z_0}{2}\right)\sin\left(\frac{n\pi Z}{2}\right)\exp\left(\frac{-n^2\pi^2}{4}\left(T-T_0\right)\right). \tag{5.39}$$

In Equation (5.38), $f(Z_0)$ is the initial condition (the parabolic distribution of pore pressures in our case).

Therefore, taking Equations (5.36) to (5.39) into account,

$$W\left(Z,T\right)=\int_0^2\left(\sum_{n=1}^{\infty}\sin\left(\frac{n\pi Z_0}{2}\right)\sin\left(\frac{n\pi Z}{e}\right)\exp\left(-\frac{n^2\pi^2T}{4}\right)\right)\left(\overline{A}+\overline{B}Z_0+\overline{C}Z_0^2\right)\mathrm{d}Z_0=$$

$$=\sum_{n=1}^{\infty}\sin\left(\frac{n\pi Z}{2}\right)\exp\left(-\frac{n^2\pi^2T}{4}\right)\int_0^2\left[\overline{A}\sin\left(\frac{n\pi Z_0}{2}\right)+\overline{B}Z_0\sin\left(\frac{n\pi Z_0}{2}\right)+\overline{C}Z_0^2\sin\left(\frac{n\pi Z_0}{2}\right)\right]\mathrm{d}Z_0=$$

$$=\sum_{n=1}^{\infty}\frac{2}{n\pi}\sin\left(\frac{n\pi Z}{e}\right)\exp\left(-\frac{n^2\pi^2T}{4}\right)\left\{\overline{A}\left[\left(1\right)^{n+1}+1\right]+2\overline{B}\left(-1\right)^{n+1}+4\overline{C}\left[\frac{2}{n^2\pi^2}\left[\left(-1\right)^n-1\right]-\left(-1\right)^n\right]\right\} \tag{5.40}$$

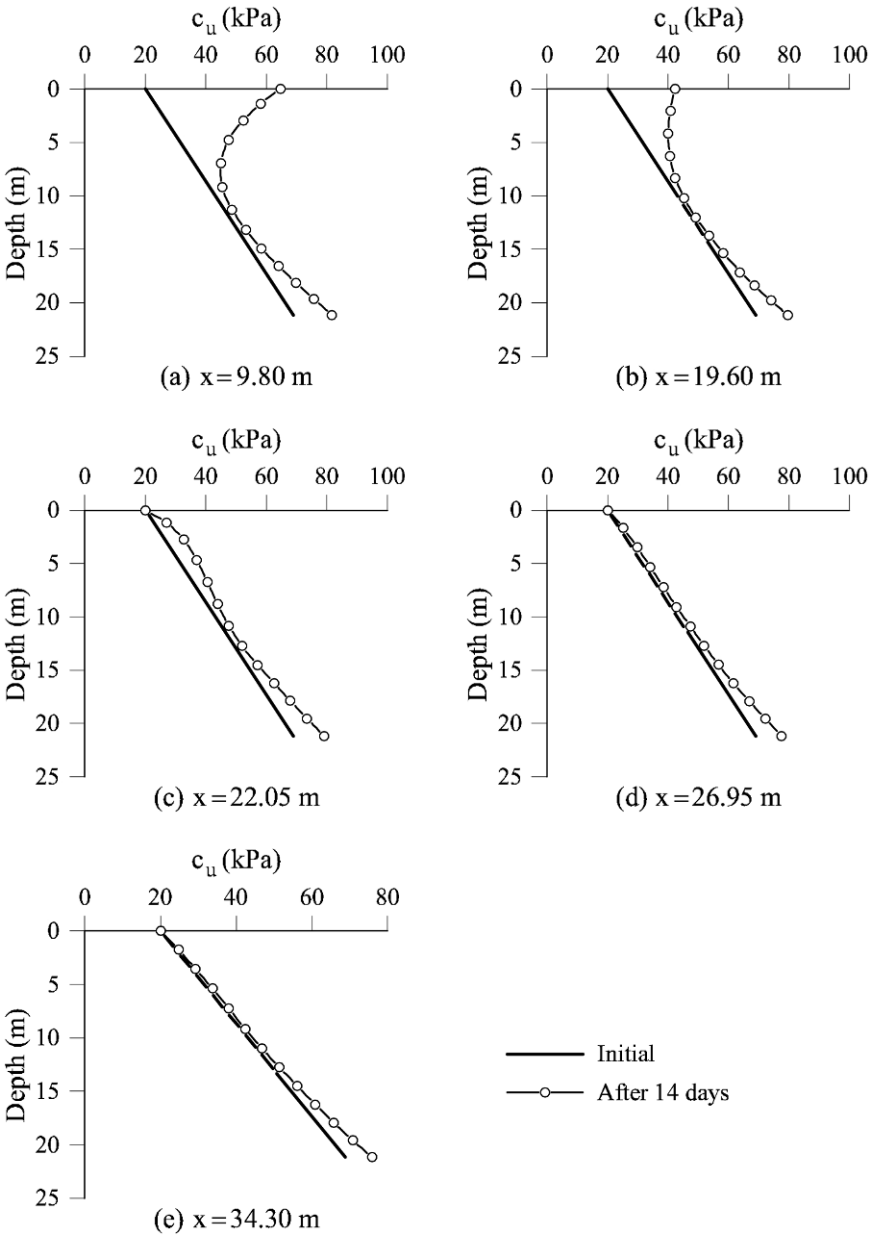

Figure 5.30 Undrained strength at the vertical profiles defined by x = 9.8, 19.6, 22.05, 26.95 and 34.30 m in Figure 5.25. Each one of the plots provides the calculated initial strength and the resulting profile 14 days after the beginning of consolidation, when caissons were still filled with water.

5.6.5 Effective stresses and updated undrained strength

Equation (5.40) was used to calculate the excess pore pressure 14 days after caisson sinking (when full of water). Adding the first five terms in Equation (5.40) provides almost the exact solution. The calculated pore water pressures are also plotted in the vertical profiles given in Figure 5.28. Fourteen days after caisson sinking, the excess pore pressure in all profiles has a similar shape with maximum values at depths ranging between 7 and 13 m. The increase in mean effective stress is calculated as

$$\Delta\sigma'_m = \Delta\sigma_m - \Delta u, \tag{5.41}$$

where $\Delta\sigma_m$ is the increment in total stress (Eq. (5.27) and profiles for $t = 0$ in Fig. 5.28) and Δu is calculated through Equation (5.40). All the necessary information is included in the plots of Figure 5.28.

The updated effective stress at $t = 14$ days is calculated by adding the initial stress state and the increment provided by Equation (5.41).

The new c_u profiles, calculated through $c_u \approx 0.25\sigma_v$, are compared with the initial values in Figure 5.30. A significant increase in c_u occurs in the first 5 m under the caisson. A smaller increase close to the lower drained boundary has a negligible effect on the increase in caisson failure load. Note also that beyond the loaded area ($x > 19.60$ m), the increase in undrained strength is very small at any depth.

The new distribution of c_u values under the caisson is now fundamentally different if compared with the initial linear increase with depth. Now c_u reaches a local maximum directly under the caisson and decreases with depth until reaching the initial distribution of undrained strength, which increases linearly with depth. This change will have interesting effects on the critical failure mechanism, as explained below.

The next step in caisson construction was increasing caisson loading to its full design value (sand filling). The safety factor against failure will now be calculated as well as the subsequent consolidation process under the new load. This will lead to an updated distribution of undrained strength, which will be operating at the time of storm arrival.

5.7 Caisson Full Weight. Safety Factor against Failure and Additional Consolidation

Consider again in Figure 5.23 the symmetric, shallow, failure mechanism (half width of the caisson). The dissipation work on the edges of the triangular wedges will be approximated by three values (two nodes and the mid point). For instance the average c_u value on segment $A'B'$ will be

$$c_u^{A'B'} = (c_u^{A'} + c_u^{1} + c_u^{B'})/3, \tag{5.42}$$

where c_u^{1} is the strength of the intermediate point between A' and B'. The calculation of the internal dissipation work follows the procedure developed

before

$$W_{\text{int}} = \left[\left(c_u^{\text{A'B'}} + c_u^{\text{B'E'}} + c_u^{\text{E'C'}} + c_u^{\text{C'D'}}\right)\right]\frac{b}{4\cos\alpha}\delta_1 + c_u^{\text{B'C'}} b\cos\alpha\delta_1 + c_u^{\text{A'E'}} b\cos\alpha\delta_1 = \\ = \left[\left(c_u^{\text{A'B'}} + c_u^{\text{B'E'}} + c_u^{\text{E'C'}} + c_u^{\text{C'D'}}\right)\frac{b}{4\cos\alpha} + \left(c_u^{\text{B'C'}} + c_u^{\text{A'E'}}\right)b\cos\alpha\right]\delta_1. \tag{5.43}$$

The external work, W_{ext}, was given in Equation (5.20). Making $W_{\text{ext}} = W_{\text{int}}$ and isolating the collapse load Q

$$Q = \frac{2}{\sin\alpha}\left(\frac{W_{\text{int}}}{\delta_1}\right). \tag{5.44}$$

The preceding Q value should be minimized with respect to α. This collapse load could be compared with the net caisson stress applied when cells are filled with saturated sand (Q/b = 220 kN/m).

An alternative failure mechanism is the non-symmetric zone sketched in Figure 5.24. Mean c_u values on segments limiting the moving triangular wedges are calculated following previous results. The internal dissipation is now given by

$$W_{\text{int}} = \frac{b}{2\cos\alpha}\left(c_u^{\text{AB}} + c_u^{\text{BE}} + c_u^{\text{CD}} + c_u^{\text{EC}}\right)\delta_1 + 2b\cos\alpha c_u^{\text{BC}}\delta_1 \tag{5.45}$$

and

$$W_{\text{ext}} = Q\sin\alpha\delta_1. \tag{5.46}$$

Therefore, since $W_{\text{int}}=W_{\text{ext}}$,

$$Q = \frac{1}{\sin\alpha}\left(\frac{W_{\text{int}}}{\delta_1}\right). \tag{5.47}$$

Again, a minimization process with respect to angle α should be performed. The two cases (symmetric and non-symmetric mechanisms) were solved in an Excel sheet following the preceding methodology and equations. The following results are obtained for t = 14 days:

Symmetric mechanism

$$Q/b = 264 \text{ kN/m}; \qquad SF = \frac{264}{220} = 1.20; \qquad \alpha = 56^{\text{o}}.$$

Non-symmetric mechanism

$$Q/b = 244 \text{ kN/m}; \qquad SF = \frac{244}{220} = 1.11; \qquad \alpha = 47^{\text{o}}.$$

The variation of the failure load with angle α for the two mechanisms is given in Figure 5.31. The critical failure mechanism is now the non-symmetric one. The reason is that a deeper non-symmetric mechanism goes in search of lower strength

values if compared with the shallower symmetric one. This is an effect of the increase in undrained strength, which is maximum at the upper dissipation boundary (where mean stresses are maximum and the drainage more effective) and decreases with depth.

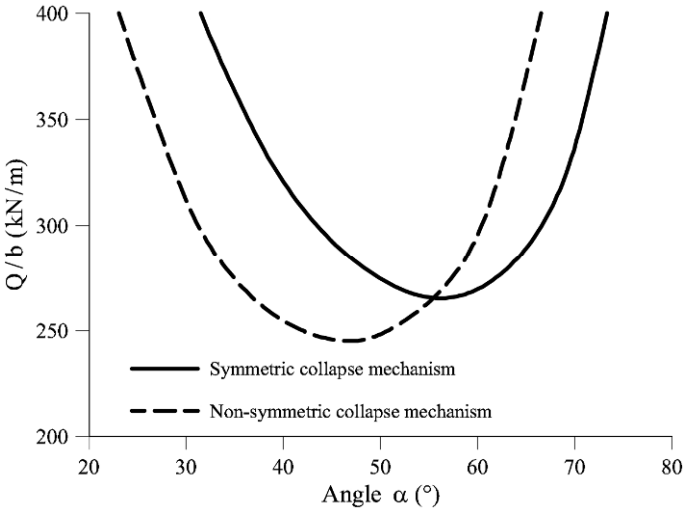

Figure 5.31 Variation of upper bound collapse load with angle α of the failure mechanism. Caisson partially consolidated under full weight.

Though the calculated minimum safety factor is small (≈ 1.1), the fact is that caissons survived also the sand filling and a new consolidation process started under the added load. This result can also be interpreted in the sense that the upper bound calculation developed is actually not that much above the true bearing capacity!

5.7.1 Caissons under full weight

The best way to analyze the consolidation in the days that followed sand filling is to imagine the process divided into two parts. The first one is simply the continuation of the consolidation induced by caisson sinking (caisson filled with water). The second one is a new process whose starting time is the application of the new load. It has been calculated before that filling the caissons with sand implied an increase in uniform load amounting to $\Delta Q/b$ = 86 kPa on the base of the caissons.

The previous analysis is repeated having in mind that the objective is now to determine the undrained strength distribution at the time of the storm arrival. Therefore, the distribution of mean stresses will now be given by Equation (5.27) for $q = Q/b$ = 220 kN/m. The pore pressures are the result of two contributions:

a) A consolidation process induced by excess pore pressures calculated for $\Delta q = \Delta Q/b$ = 134 kN/m, lasting for t = 21 days.

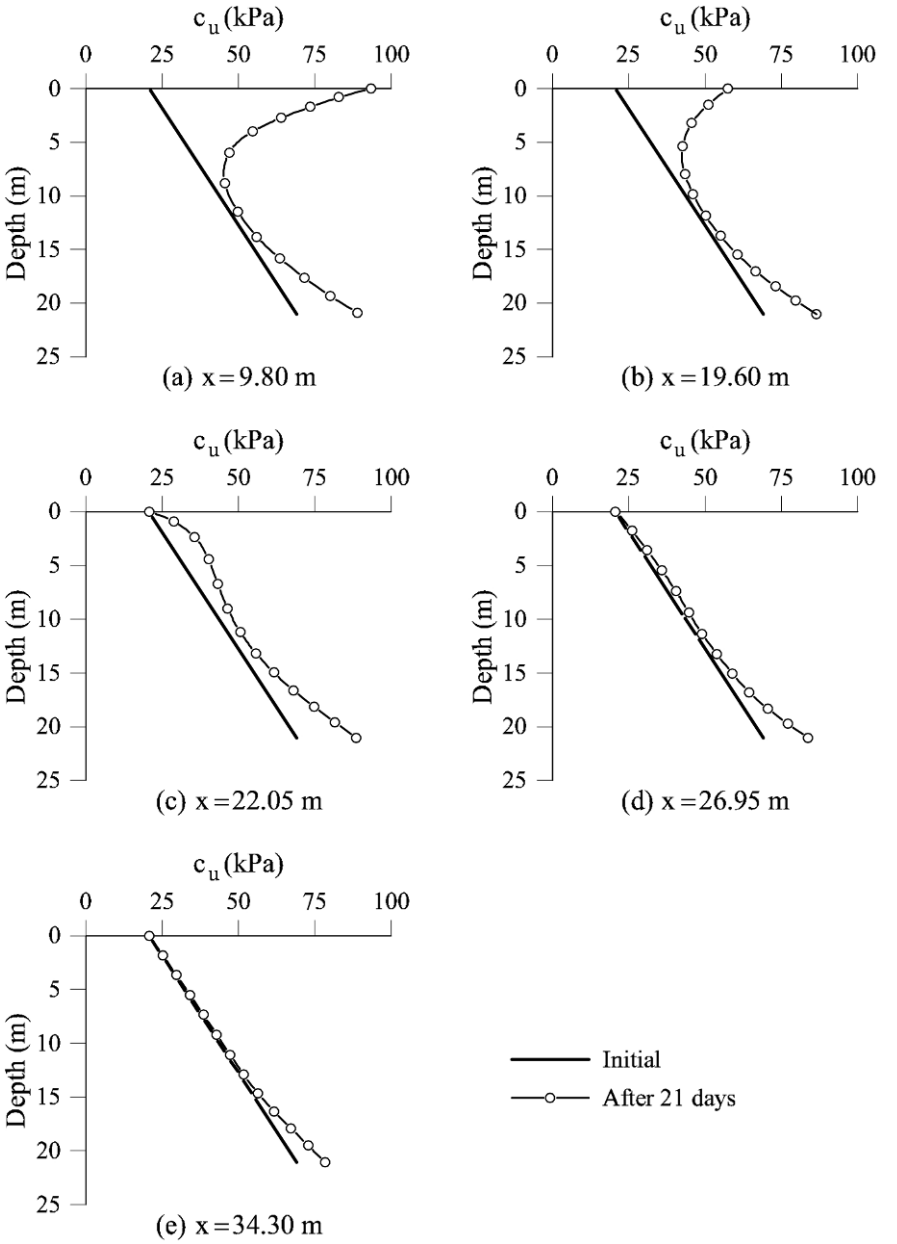

Figure 5.32 Undrained strength at the vertical profiles defined by x = 9.8, 19.6, 22.05, 26.95 and 34.30 m in Figure 5.25 at the time of storm arrival (t = 21 days after caisson sinking). Also indicated is the initial distribution of c_u.

b) A consolidation process induced by excess pore pressures calculated for $\Delta q = Q/b = 86$ kN/m, lasting for $t = 7$ days.

The analysis follows steps previously described and is not repeated here. The resulting distribution of undrained strength is calculated as follows

$$c_u(21 \text{ days}) = c_u(\text{initial}) + \Delta c_u(t = 21 \text{ days; water filled caissons}) + \Delta c_u(t = 7 \text{ days; sand filled caissons}). \quad (5.48)$$

The result of this calculating process is given in Figure 5.32. It shows the resulting current profiles of undrained strength and the initial distribution of c_u for a few vertical profiles characterized by the horizontal coordinates x = 9.8, 19.6, 22.05, 26.95 and 34.30 m (Fig. 5.25). The added load (sand filling) had a limited time to be transformed into effective stresses and, accordingly, into available undrained strength. Nevertheless the upper levels of the foundation soil under the caisson significantly increased the undrained strength. The strength profile shows a maximum at the caisson-foundation contact. Strength decreases rather fast with depth to meet the initial values which increase linearly with depth. This distribution is plotted in a two-dimensional cross-section in Figure 5.33. It shows that caisson consolidation was able to build a "strong" soil nucleus in the upper 7 m although strength decreased continuously with depth. Beyond a depth of approximately 10 m, the initial undrained strength is recovered. A small increase in strength is calculated in the vicinity of the lower drainage layer.

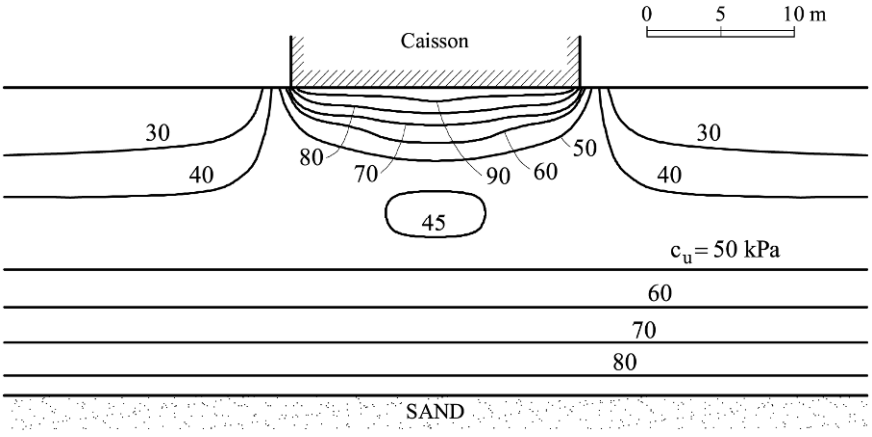

Figure 5.33 Calculated distribution of available undrained strength at the time of storm arrival (November 11, 2001).

The following vertical collapse loads and safety factors were calculated for the strength distribution shown in Figure 5.33,

a) Symmetric mechanism: $q_{\text{collapse}} = Q/b = 313$ kN/m for $\alpha = 58°$,

$$SF = \frac{313}{220} = 1.42;$$

b) Nonsymmetric mechanism: $q_{collapse} = Q/b = 269$ kN/m for $\alpha = 44°$,

$$SF = \frac{269}{220} = 1.22;$$

This was the situation when the eastern storm of November 11, 2001 hit the caissons.

Note that the critical mechanism is now clearly the deep (nonsymmetric) one. The lower failure surface reaches in this case a depth of 9.46 m, against a maximum depth of 6.72 m for the symmetric, shallower mechanism. This is a consequence of the "inverted" profile of undrained strength created by the caisson weight.

5.8 Caissons Under Storm Loading

5.8.1 Wave forces on caissons

A well-known calculation method to find wave forces on vertical dykes was proposed by Goda (1985). The wave load has two components: an excess pressure on the exposed wall and an uplift pressure on the caisson base. The assumed distribution of these pressures is shown in the sketch of Figure 5.34.

The pressure distributions are equivalent to the concentrated forces:

- Horizontal force H at an elevation Z_H.
- Uplift force U at a horizontal coordinate $X_U = 1/3b$.

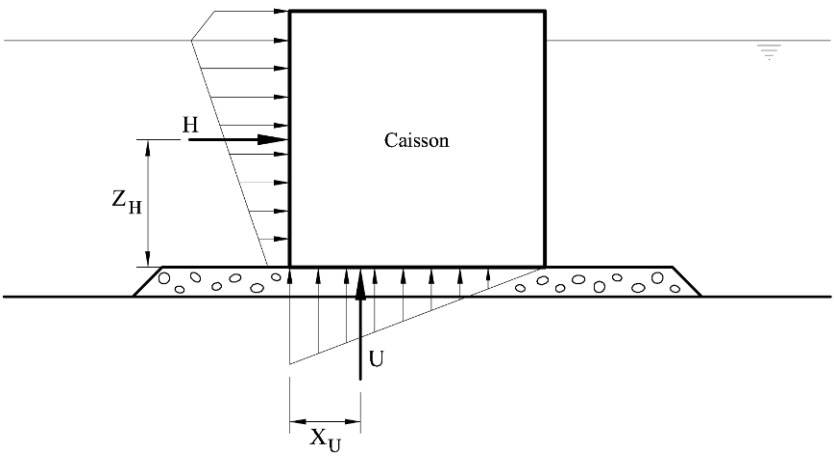

Figure 5.34 Goda's wave pressures.

Goda's formula is detailed in the Appendix to this chapter. For the maximum significant wave height recorded in the storm of November 11, 2001 (see Fig. 5.3), the following forces and points of application are calculated

$H = 779$ kN/m, $Z_H = 8.94$ m,

$U = 267$ kN/m, $X_U = b/3 = 6.5$ m.

The uplift force U reduces the net weight of the caisson. The objective now is to estimate the stability conditions of the caisson under this new set of forces. Wave forces are cyclic, though, and therefore two analyses will be made. First the static stability of the caisson being acted by the highest static forces (H and V) induced by the storm waves will be explored. Then the issue of the soil liquefaction under repeated wave loading will be examined.

5.8.2 Static analysis. Safety factor

The problem is represented in Figure 5.35. The weight Q is now reduced by the calculated uplift force U and a horizontal wave loading H is added. The assumed failure mechanism for the application of the upper bound theorem is also shown. Under the virtual displacement rate δ_1 of the wedge under the caisson, only the vertical force Q_r and the horizontal force H perform external work. Note that in this case, the symmetric mechanism is no longer possible and only the non-symmetric "deep" mechanism will be analyzed. The external work is written

$$W_{\text{ext}} = (Q - U)\delta_1 \sin\alpha + H\delta_1 \cos\alpha. \tag{5.49}$$

The internal dissipation work follows previous developments. Since the soil has a marked non-uniform distribution of undrained strength, the calculations are based on the c_u values estimated at the corners of the mechanism (A, B, C, D, E) and at the mid points (1, 3, 4, 5, 6). Note also that the caisson and the wedge ABE displace as a solid body and therefore no shear dissipation occurs on AE. The dissipation work is therefore given by Equations (5.45) and (5.42).

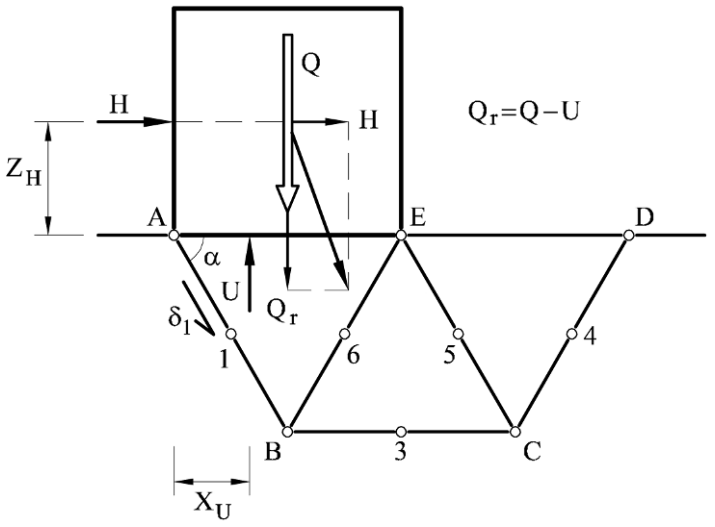

Figure 5.35 Failure mechanism under combined gravitational load and static wave forces.

Now the determination of the safety factor against failure requires more careful consideration. So far in this chapter, the safety factor has been defined as the ratio between the limiting vertical load (determined through the upper bound theorem) and the actual load induced by the caisson defined by its own weight. But now three different forces are acting on the caisson: weight Q, horizontal load H and uplift U.

We will distinguish the real forces from the forces actually inducing the failure (Q^{real} vs Q^{failure}, etc). A single safety factor SF is defined as follows:

$$SF = \frac{Q^{\text{failure}}}{Q^{\text{real}}} = \frac{H^{\text{failure}}}{H^{\text{real}}} = \frac{U^{\text{failure}}}{U^{\text{real}}}. \tag{5.50}$$

The upper bound equilibrium equation ($W_{\text{ext}} = W_{\text{int}}$), which defines the failure loads, may be written as follows:

$$SF\left[\left(Q^{\text{real}} - U^{\text{real}}\right)\sin\alpha + H^{\text{real}}\cos\alpha\right] = \frac{W_{\text{int}}}{\delta_1} = W_{\text{int}}^{*}. \tag{5.51}$$

This equation defines the safety factor as

$$SF = \frac{W_{\text{int}}^{*}}{(Q^{\text{real}} - U^{\text{real}})\sin\alpha + H^{\text{real}}\cos\alpha}. \tag{5.52}$$

W_{int}^{*} is a function of α and the minimization of Equation (5.52) with respect to α will provide the best upper bound approximation to SF.

Consider now the structure of W_{int}^{*} given in Equation (5.45). It is, in fact, a weighted sum of c_u values taken at different positions (c_{uj}) (the nodes of the mechanism and the auxiliary intermediate points)

$$W_{\text{int}}^{*} = \sum_{j=1}^{N} \beta_j c_{uj}, \tag{5.53}$$

where β_j are coefficients which depend on the geometry of the mechanism. Therefore, Equation (5.51), which establishes the balance between external work and internal dissipation, can be written

$$SF\left[(Q^{\text{real}} - U^{\text{real}})\sin\alpha + H^{\text{real}}\cos\alpha\right] = \sum \beta_j c_{uj} \tag{5.54}$$

or

$$(Q^{\text{real}} - U^{\text{real}})\sin\alpha + H^{\text{real}}\cos\alpha = \sum \beta_j \frac{c_{uj}}{SF} = \sum \beta_j c_{uj}^{*}, \tag{5.55}$$

where

$$c_{uj}^{*} = \frac{c_{uj}}{SF} \tag{5.56}$$

is the set of mobilized undrained shear strengths necessary to satisfy the balance implied by the upper bound mechanism in terms of the actual real loads.

But this definition is essentially similar to the safety factor concept used in limit equilibrium analysis, i.e., the reduction factor which has to be applied to the strength parameters in order to achieve strict equilibrium under the actual real loads.

The fact that the safety factor defined in (5.50) as a ratio of loads becomes a strength reduction factor in (5.56) is simply a consequence of the linear relationship between failure loads and undrained strength. This is the case in undrained stability analysis but it is far from being so in drained analysis because failure loads and the ($\tan\phi'$) drained strength parameter are not linearly related.

The expression (5.56) has to be seen as a sound "geotechnical" definition of safety factor. It is equivalent to loading ratios (Eq. (5.50)) only under conditions of undrained analysis.

But the safety factor is not a theoretical or particularly well-defined measure of uncertainty. Other alternatives may suit the needs of the designer. For instance, in the case discussed now, it may be argued that the wave loading is rather uncertain compared with the caisson weight Q^{real}. It may be also accepted that the soil undrained strength is well known. Then, a safety factor aimed at judging the risk of failure induced by wave loading may be defined as

$$SF^{*} = \frac{H^{\text{failure}}}{H^{\text{real}}} = \frac{U^{\text{failure}}}{U^{\text{real}}}. \tag{5.57}$$

Then, following the previous steps, SF^{*} is obtained as

$$SF^{*} = \frac{W_{\text{int}}^{*} - Q^{\text{real}} \sin\alpha}{H^{\text{real}} \cos\alpha - U^{\text{real}} \sin\alpha}. \tag{5.58}$$

This function of α should be now minimized, following the procedures associated with the upper bound theorem.

Safety factors *SF* and SF^{*} were calculated for the following set of forces: Q^{real} = 4,312 kN/m; H^{real} = 779 kN/m; U^{real} = 267 kN/m and for the calculated distribution of c_u values at the time of the storm arrival (t = 21 days after first sinking).

The calculated Safety Factors and angle α, which defines the mechanism, are

$$SF = 1.10 \quad (\alpha = 41^{\circ}), \quad SF^{*} = 1.77 \quad (\alpha = 41^{\circ}).$$

The calculation indicates that the static wave force was not enough to induce a generalized failure of caissons but it was quite close, if one considers the classical definition of safety factor (Eq. (5.56)). It is worth reminding that our upper bound mechanisms provide estimates that are pretty close to the true ones: after the caisson sand filling we also predicted the *SF* = 1.1 and the fact was that the

caissons did not fail!

The fact that SF^* is a high value indicates that the scale to measure risk should be based on a given definition of safety factor. If the definition changes, we should be prepared to change the scale of risk. In this book Safety Factor is a strength reduction factor, as defined, for undrained conditions, in Equation (5.56).

The deep failure of caissons was also an indication that the foundation soil had experienced an additional reduction in strength most likely associated with soil liquefaction. The next section deals with the liquefaction of the foundation soil.

5.8.3 Analysis of liquefaction

Stability of caissons subjected to horizontal loading is checked in practice by examining a few failure possibilities: bearing capacity (or overall stability), sliding on its base and overturning. In the preceding section the bearing capacity of caissons against its own weight, combined or not with a static estimation of wave loading, has been discussed. The survey after the failure did not provide any support for sliding or overturning modes of failures.

The deep sinking of caissons after the failure (Fig. 5.5) and the type of failure (tilting of caisson top in the seaward direction) suggest that soil liquefaction played a significant role in the failure. The cyclic interaction diagram (Fig. 5.13) shows that liquefaction conditions are defined by the static or average shear stress ratio, the cyclic ratio, and the number of applied cycles.

Instead of performing a comprehensive dynamic analysis, the following simplified approach will be followed here:

a) Shear stresses on horizontal planes (τ_{xz}) will be computed on the foundation for the following two states:

a1) caisson weight;

a2) wave action.

The theory of elasticity will be used in these calculations.

b) Stress ratios (shear stress over vertical effective stress) will then be calculated. The distribution of vertical effective stresses (σ'_z) corresponds to the consolidation time at the time of storm arrival (t = 21 days after caisson sinking).

c) The calculated stress ratios will be compared with the information provided by the cyclic interaction diagram (Fig. 5.13). For the estimated number of loading cycles applied by the storm, points in the foundation soil may either fall in a stable zone or in an unstable (liquefied) domain. Points "satisfying" the liquefaction condition will define an area where undrained soil strength will decrease to a post liquefaction state.

d) A new stability analysis following the upper bound methodology will be carried out. The spatial distribution of undrained strength will now be a consequence of the initial state (linear increase of c_u with depth), the previous consolidation history under caissons weight, and the c_u reduced values on the liquefied areas.

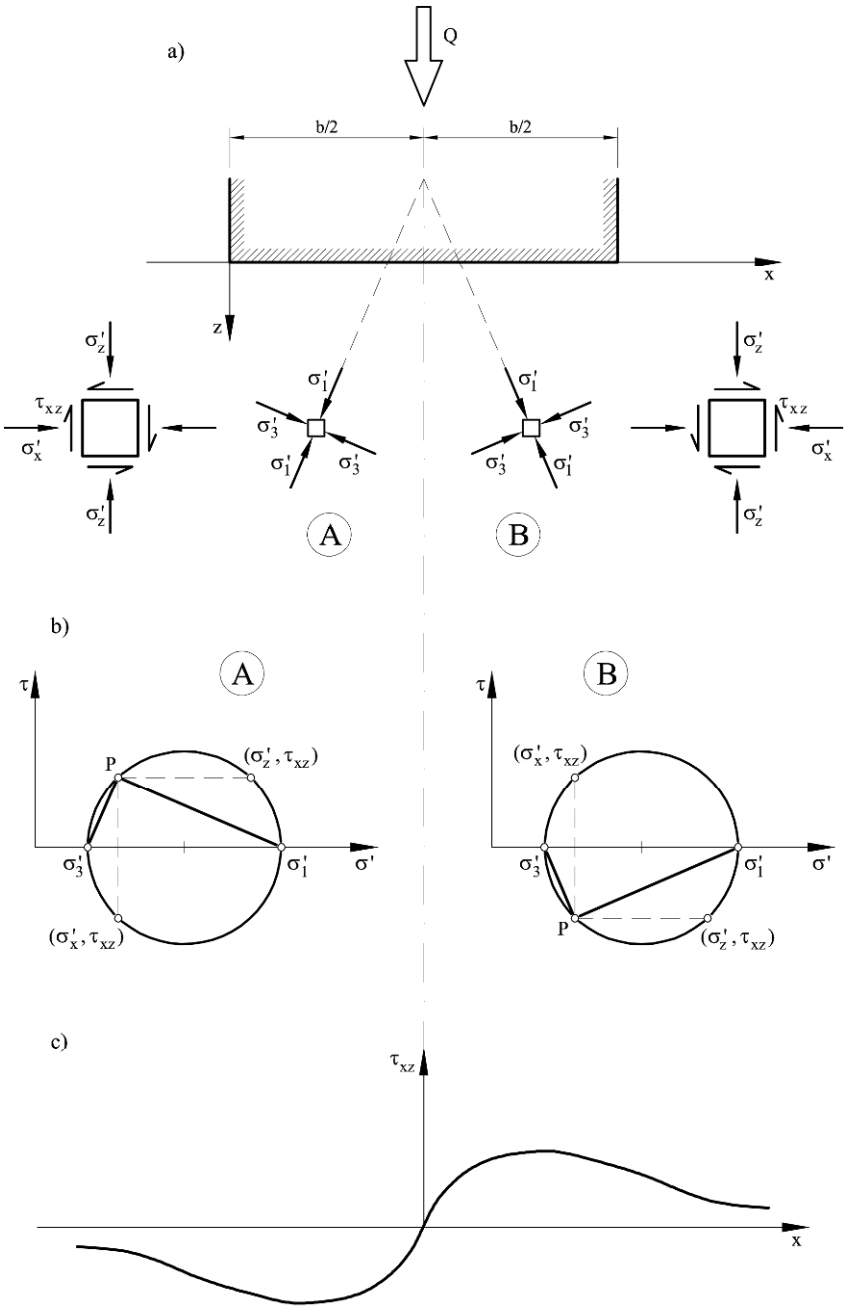

Figure 5.36 (a) Stress distribution under the caisson weight; (b) Mohr diagrams; (c) distribution of shear stresses on a horizontal plane.

a) Shear stresses on horizontal planes

Consider the stress distribution under the caisson induced by its own weight. A descriptive representation of the principal stresses inside the ground is given in the sketches of Figure 5.36. The major principal stress is directed towards the axis of the load, on the surface. Two points are indicated in the figure (A and B) symmetric with respect to the caisson axis. The two Mohr circles on the same figure (Fig. 5.36b) provide the normal and shear stresses on any plane through points A or B. The circles are oriented by means of the pole P, also plotted in the figure.

In point B, the shear stress τ_{xz} on horizontal planes is directed in the direction of the increasing x coordinate. However, in the symmetric point A, τ_{xz} has the opposite sign. On the vertical caisson axis, the major principal stress is vertical and the shear stresses on horizontal or vertical planes are zero.

Therefore, the caisson vertical loading induces a distribution of shear stresses on horizontal planes which is point-symmetric with respect to the origin of the plot (Fig. 5.36c). At the origin the shear stress is zero and at increasing x distance (in both directions, negative and positive), away from the caisson foundation area, they will eventually vanish. Therefore, the shear stress, when plotted along straight lines parallel to the x-coordinate, will start at zero at $x = b/2$ and it will find a maximum at some given distance from the axis to decrease again with distance. The plot in Figure 5.36c is a qualitative representation of τ_{xz} on a horizontal axis that follows the preceding observations.

The distribution of τ_{xz} beneath a uniformly loaded infinite strip was given in Equation (5.26d). The calculated shear stress on several horizontal planes under the caisson weight, immediately before the storm, is given in Figure 5.37. These shear stresses are regarded as the static permanent shearing in the ground. Note that the initial geostatic states, where effective principal stresses follow the vertical and horizontal directions throughout the soil, do not introduce any shearing on horizontal planes.

Note the skew-symmetric distribution of shear stresses, and the existence of a maximum/minimum at some distance from caisson axis, as predicted. Close to the foundation surface, a sharp peak is calculated at the transition between the loaded and the unloaded areas. Away from that zone of intense shearing, the absolute value of the shear stress is small. At depth, the peak "widens" and the shear stresses distributes more evenly. The caisson weight induces significant shear stresses at depth. Even at a depth of 20 m, where the sandy stiff layer marks the lower boundary of the silty foundation soil, the maximum shear stress is close to 40 kPa.

The fact that a shear stress is positive or negative is not of particular significance here because they are equally capable of inducing limiting conditions (isotropic soil properties are assumed).

Consider now the wave action in Figure 5.38. The resultant horizontal force H acting at a height Z_H over the caisson base is made equivalent to a shear force H at the foundation base and a moment $M_H = H \cdot Z_H$. A triangular distribution of

water overpressures at the caisson-soil interface is also acting, following Goda (1985). It is equivalent to a uniform uplift load U and a moment M_U, which adds to M_H. The value of these forces for the storm of November 11, 2001 is calculated in the appendix.

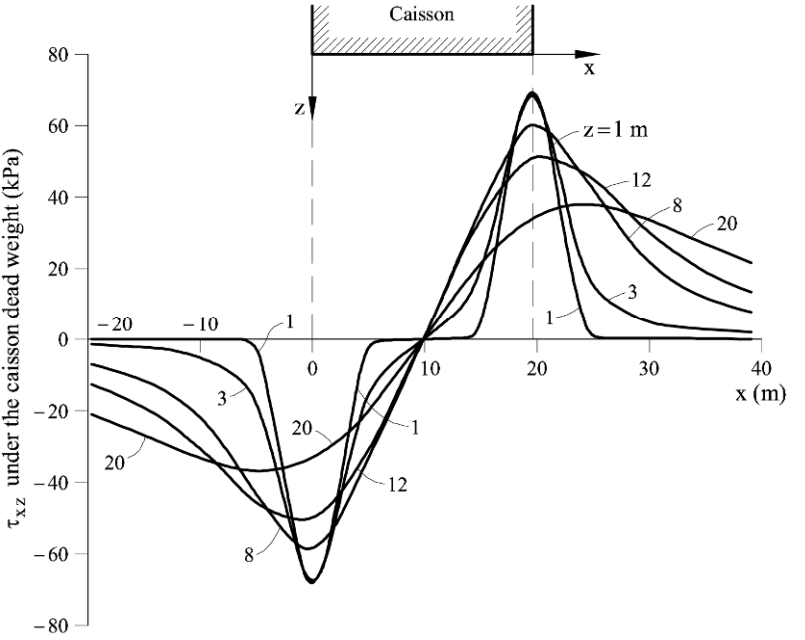

Figure 5.37 Calculated τ_{xz} values under the caisson dead weight at depths z = 1, 3, 8, 12 and 20 m.

The set of wave induced forces is equivalent to the following set of stresses on the caisson foundation interface:

I: A shear stress $q = H/b$ in the direction of H;

II: A uniform uplift stress $p = U/b$;

III: A uniform uplift stress $p_1 = \sigma_{max} = 6M/b^2$, where $M = M_H + M_U$;

IV: A triangular distribution of normal compression stresses with maximum value $p_2 = 2\sigma_{max} = 12M/b^2$.

Stress distributions inside the soil for cases II and III were already given in Equation (5.26). Poulos and Davis (1973) also provide an elastic solution for Cases I and IV. The shear stress τ_{xz} for these two loading cases is given in Figure 5.38c.

Figure 5.39 shows the calculated shear and normal stresses for the following cyclic forces H = 779 kN/m; $M_H = H \cdot Z_H$ = 7,242 kN·m/m, U = 267 kN/m; M_U = 869 kN·m/m. These values are taken from the appendix. Now the skew-symmetry of shear stress distribution is lost. However, the peak values for shallow depths

concentrate again in the vicinity of the caisson edges. In addition, the shearing force applied at the interface results in significant shear stresses at shallow depths, under the caisson base. Cyclic shear stresses are of the same order of magnitude as static shear stresses.

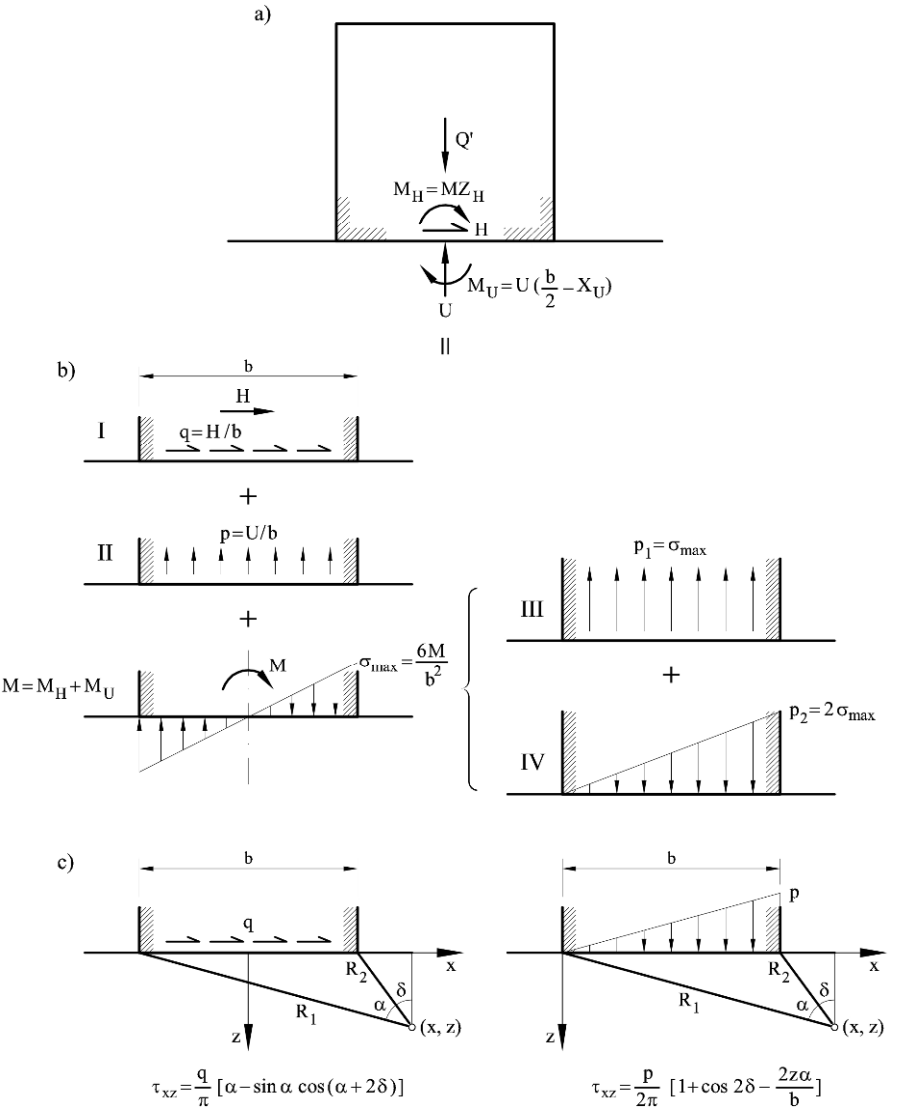

Figure 5.38 (a) Forces in caisson in the presence of wave loading; (b) stresses on the caisson-foundation interface; (c) shear stresses, τ_{xz}, in the subsoil induced by uniform distribution of boundary shear forces and a triangular normal loading.

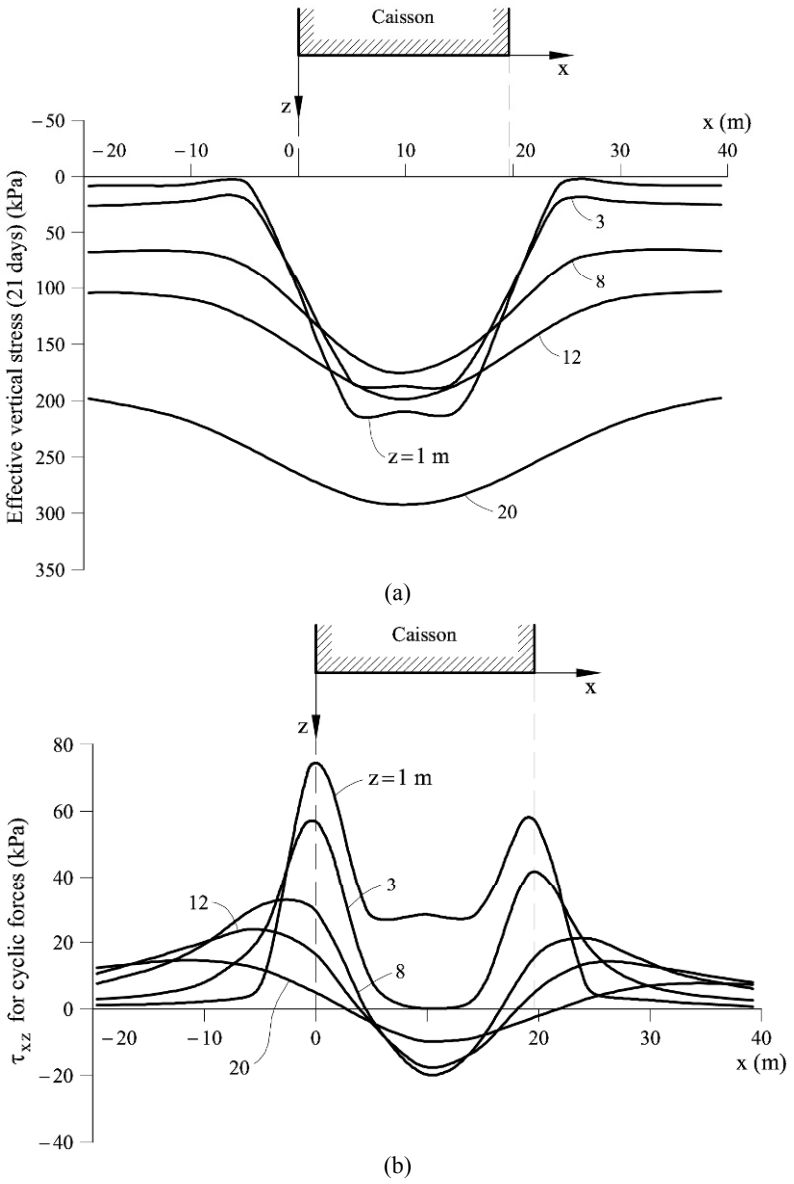

Figure 5.39 Calculated (a) static effective vertical stress σ'_v and (b) cyclic shear stress τ_{xz} at depths z = 1, 3, 8, 12 and 20 m.

b) Stress ratios

Normal effective stresses on horizontal planes were calculated previously. Since they are required to normalize shear stresses, they have been plotted on similar

positions in Figure 5.39b. A vertical profile is also given in Figure 5.40 to point out that vertical effective stresses reach a high value close to the caisson base (because of the full consolidation at shallow depths). They decrease with depth down to a depth of about 7 m and increase when the geostatic weight – initial state – dominates again.

The ratios τ_{ave}/σ'_v and τ_{cycl}/σ'_v are now calculated. They are plotted for the same depths in Figure 5.41a,b. The two figures show that stress ratios reach very high values, at shallow depths, in the transition zone between loaded and unloaded areas. Of course, these high stress ratios cannot be resisted by the soil and stress redistributions will occur. The figure indicates, however, that these shallow zones at the edge of caissons are plastified and, in addition, they are particularly critical against cyclic loading. Under the caisson, the stress ratio decreases rapidly due to the high confining stress. At increasing depths the transition between loaded-unloaded surface areas remains in critical conditions. This is better appreciated if the stress ratios in Figure 5.41 are compared with the cyclic interaction diagram in Figure 5.13.

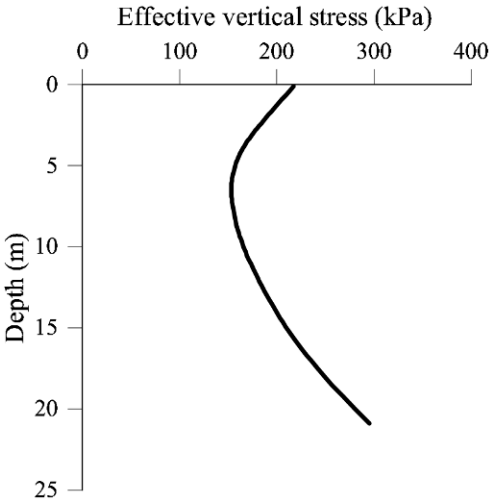

Figure 5.40 Effective vertical stresses at $t = 21$ days after caisson sinking at $x = 14.70$ m.

c) Liquefied zones

Calculated stress ratios were compared with the cyclic interaction diagram given in Figure 5.13. Stress ratios falling on the unstable or liquefied zone have bean indicated in Figure 5.42. The "stable" zone is defined in a simplified manner by the two conditions $\tau_{cycl}/\sigma'_v < 0.15$ and $\tau_{ave}/\sigma'_v < 0.25$. Outside this rectangular domain, the soil is assumed to reach liquefaction. The limiting cyclic stress ratio (0.15) is approximately valid for a number of cyclic stress applications of 100 – 200. This is close to the number of wave impacts when the storm reaches its maximum intensity (a significant wave height of 4 m).

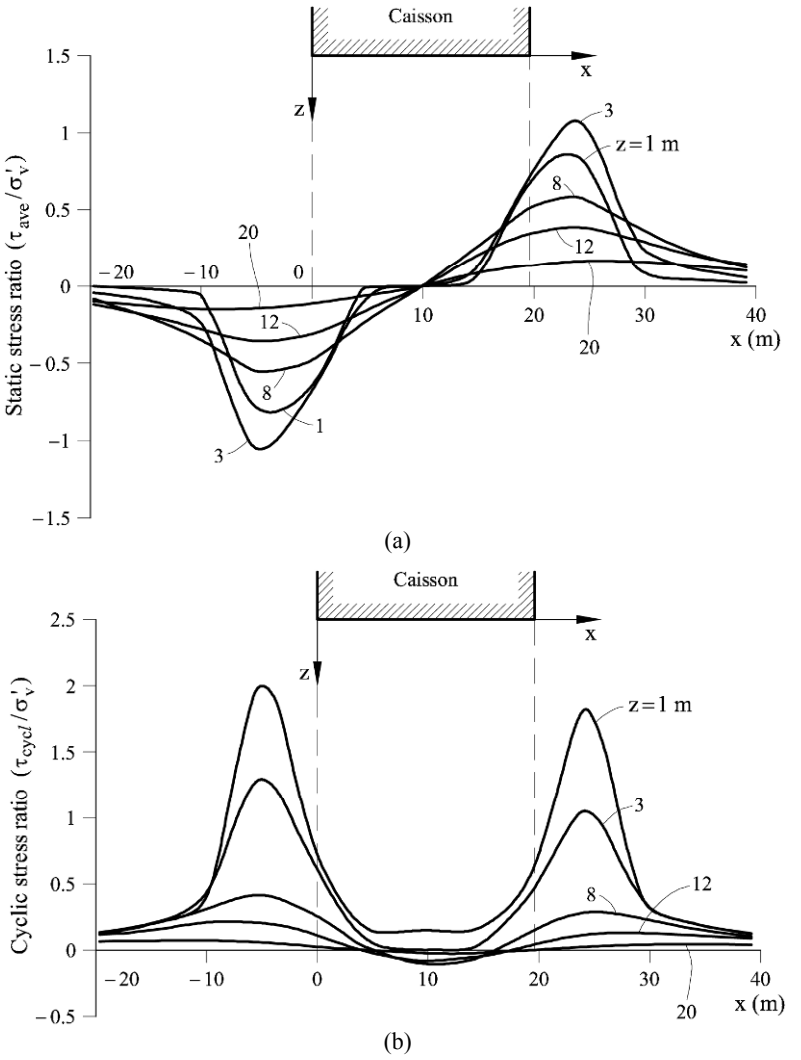

Figure 5.41 (a) Static (or average) stress ratio; (b) cyclic stress ratio.

The liquefied areas define two wide bulbs on both edges of the caisson. They reach a maximum depth of about 14 m. Under the caisson central area, however, no liquefaction conditions develop (Fig. 5.42).

The undrained strength of the liquefied areas was given in Figure 5.14. The scatter is high and it is difficult to select a value with some confidence, but a post liquefaction strength close to the maximum suggested by this plot $c_u = 0.06\sigma'_v = 0.09\sigma'_m$ was adopted to estimate the stability in the case of soil liquefaction.

d) Stability of caissons

The final step of the analysis is to calculate the failure conditions when part of the foundation soil is liquefied. The failure mechanism crosses the liquefied zone located on the leeward side of the caisson foundation (Fig. 5.42). In the non liquefied areas, the distribution of undrained strength was reported before. Within the liquefied area $c_u = 0.09\sigma'_m$.

The calculated safety factor, defined as in Equation (5.52), drops to 0.56 for a critical mechanism defined by an angle α = 44º. Even if the liquefaction zone is characterized by a relatively high value of the residual undrained strength ($0.09\sigma'_m$), the drop in safety factor is very significant.

If a more substantial reduction of strength is specified, the safety factor drops to very low values. This result helps to explain the deep burial of caissons as a consequence of the failure.

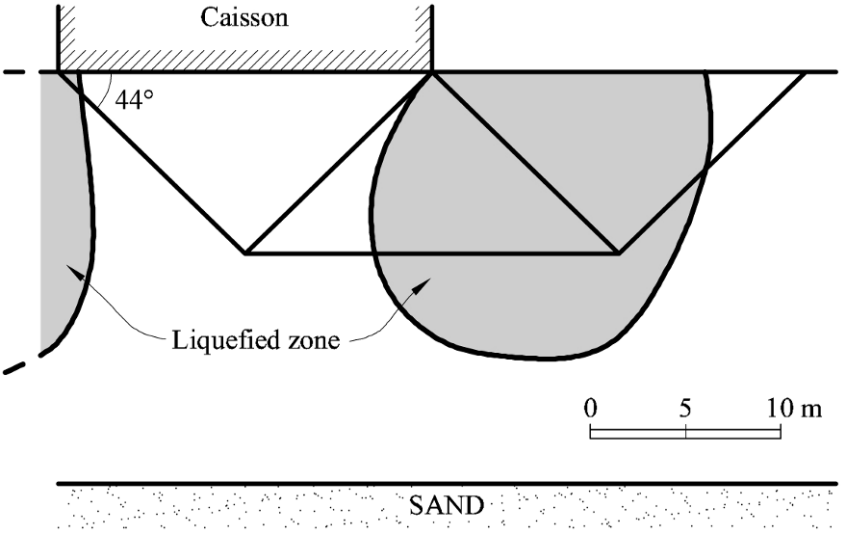

Figure 5.42 Liquefied areas under a caisson induced by storm cyclic loading. Also indicated is the critical failure mechanism.

5.9 Discussion

The upper bound theorem of plasticity provides an unsafe estimate of bearing capacity. A comparison against the available analytical solution for increasing undrained soil strength shows that errors may be in the order of 17% for the failure mechanism selected here. The mechanism is, however, simple and it may accommodate, at a limited effort, complicated spatial distributions of undrained shear strength. Consider, however, this limitation from a different perspective. Figure 5.43 shows the variation in time of the safety factor of the caissons, starting at the time of caisson sinking (t = 0) and ending at the failure time, 21 days later.

Symmetric (shallower) and non-symmetric (deeper) mechanisms are considered when appropriate. The plotted variation of safety factor with time follows the minimum values

The calculated safety factors, taking the upper bound solution as a correct estimate, should be regarded in sequence, paying attention to the changes in *SF* but not to its precise values. Its evolution in time is the most valuable information. The fact that caissons did not fail during the first sinking provides a reference condition ($SF > 1$) for $t = 0$, irrespective of calculations. Presumably, in view of the results obtained, the actual value of *SF* was in the vicinity of 1.3. Then the calculation process described, which maintains the failure mechanism, results in a *SF* value, at $t = 21$ days and for a static equivalent loading to wave action, which is greater but close to one.

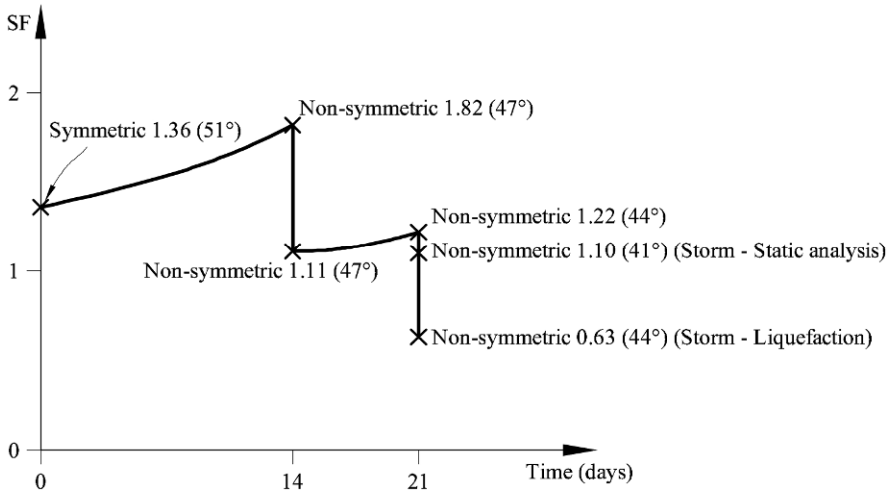

Figure 5.43 Evolution of caisson safety factor (*SF*) against bearing capacity failure. The value in parenthesis indicates the critical α angle of the failure mechanism.

Therefore, it is concluded that the failure and the deep sinking of caissons should be explained by a strength-loss mechanism associated with the cyclic wave loading. A soil liquefaction phenomenon seems a good candidate to explain the strength loss, especially if one considers the deep burial of failed caissons into the foundation soil. Of course, the silty deltaic deposits seem prone to liquefy in view of the accumulated experience synthesized in Figure 5.13. The consideration of liquefaction, which was analyzed by a procedure inspired in the cyclic mobility diagram of the natural soil, indicates that extensive zones of the caisson foundation soils reached critical conditions under the storm of November 11, 2001. A substantial reduction in safety factor is calculated, even if the loss of undrained strength is moderate. In other words, irrespective of the safety factor at $t = 21$ days under a pseudostatic wave loading, the liquefaction of the foundation soil is capable of inducing a catastrophic failure. These comments help to accept the upper bound calculation as a useful and simple procedure to analyze the

conditions and reasons for the failure, even if some error is experienced in the actual estimation of failure load.

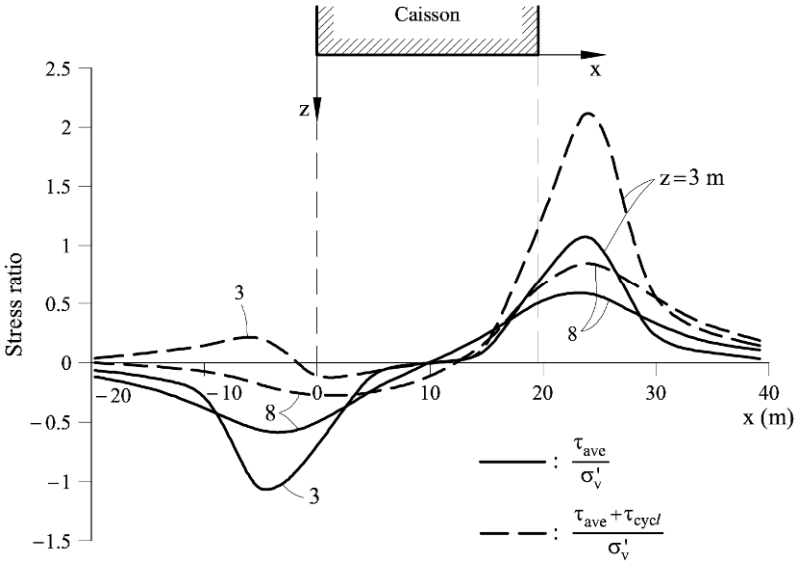

Figure 5.44 Distribution of average and maximum stress ratios.

Regarding Figure 5.43 some uncertainties remain on the exact timing of sand filling. But this is not particularly relevant because the caissons did not fail under the full weight. If a shorter time elapsed between water filling and sand filling and this shortened interval had led to $SF < 1$ at the time of sand filling operation, it simply implies that the initial SF was somewhat higher than the value calculated here. The procedure developed can be applied to a different sequence of events.

The kinematic mechanisms analyzed in this chapter imply a vertical displacement of caissons. The actual failure mechanism involved also a rotational component (see Fig. 5.5) perhaps associated with soil liquefaction. The mechanisms selected are only an approximation but they are capable of explaining in a satisfactory manner the sequence of events which led to the failure.

The liquefaction analysis has also limitations. The large stress ratios calculated in some localized areas of the foundation (in the vicinity of the caisson's edges) cannot possibly occur because soil yielding would redistribute the stress field. But classical elastic stress distributions (which are independent of elastic constants for homogeneous soil profiles) provide a reasonable approximation for extended areas of the foundation soils.

On the other hand, the plots of average static stress ratios and of the maximum stress ratios (average + cyclic) in Figure 5.44 indicate that, in some zones of the foundations soil, shear stress reversals did occur. In fact, it has been found that shear stress reversals (changing sign of τ_{xz}) lead to a more efficient and rapid development of liquefaction conditions (see Section 5.12 on Advanced Topics

below). The testing program leading to the cyclic interaction diagram of Figure 5.13 did not consider shear stress reversals and this may be also a source of error. In this case, actual field conditions seem somewhat more critical than experimental ones.

The "signature" of wave impact loading is known to be far from a regular sinusoidal or regular variation of stress, as imposed in cyclic simple shear tests. Figure 5.45 shows the time development of impact forces for a storm of a significant wave height of 11 m (Alonso and Gens, 1999). These are different conditions but the plot indicates that field impacts tend to concentrate on short time intervals. In the remaining time, within the wave period, wave forces remain small. This is also a difference between laboratory testing and field conditions.

The four failed caissons were essentially isolated and surrounded by open sea conditions. Therefore, only wave forces in the landward direction should be considered. If caissons protect a water body, the wave trough results in an unbalanced hydrostatic load in the seaward direction. This load, which enhances stress reversals, was unlikely in this case.

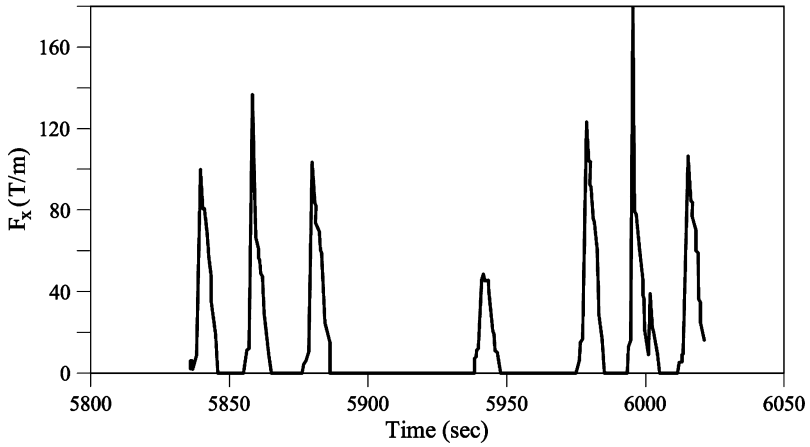

Figure 5.45 Partial record of impact wave forces against a dyke (Alonso and Gens, 1999 © 1999 Taylor and Francis Group. Used with permission).

5.10 Mitigation Measures

The failure could have been avoided by one or more of the following mitigation measures:

5.10.1 Increasing the consolidation time under caisson weight

Then the undrained strength of the natural soil would increase as well as the safety factor. However, if nothing else is changed in the design, the risk of failure remains high because the time of storm arrival is not under control. If caissons are sunk in place at, say, the beginning of summer time in the Mediterranean environment of Barcelona, chances are that no strong storms will hit the works for a few months. Then a high degree of consolidation will be achieved. It remains to

be checked if a design storm is resisted in this case. But, most probably, it will not be the case if liquefaction develops.

5.10.2 Increasing the size of the granular berm

Both its thickness and its lateral extension should be properly designed. Increasing the thickness adds a drained frictional resistance to any potential failure surface crossing the granular layer. Increasing the lateral extent increases the size of the potential failure surface or forces it to cross the granular berm. This is a good solution but there are a few remarks which should be taken into account:

- Increasing berm thickness without previous dredging may impair navigation requirements around caissons.
- Dredging soft, normally consolidated soils, requires very gentle slopes (around 1:10) to ensure stability. Environmental issues (water contamination) should be addressed.
- If dredged materials are substituted by a granular layer, the undrained strength of the underlying natural soil is essentially unchanged because effective stresses will not change much (unit weights of granular soil and a soft clayey soil are similar).
- Consolidation times are reduced significantly if vertical drains at close spacing (say 1 – 3 m) are installed in advance to any overloading.

5.10.3 Improving foundation soils

This is an expensive option. Preloading would increase c_u but this is a lengthy and costly operation in a sea environment. It has associated drawbacks (impairing navigation, increasing turbidity of waters). Soil strength may also be improved by other techniques: installing piles or granular columns or performing a dynamic consolidation by pounding the soil.

5.10.4 Increasing caisson width

Increasing the caisson width contributes to increase in the bearing capacity and it also reduces the risk of liquefaction. But the improvement is relatively small and significant increases in caisson width will be required to guarantee adequate safety.

5.10.5 After the failure

Caissons were demolished “in situ” by repeated hammering by a falling dead weight operated from a floating barge. Then they were covered by a random rockfill. An embankment-type of breakwater was finally built on the position of Caissons 1 to 4. The buried part of failed caissons remained in place.

5.11 Lessons Learned

5.11.1 Foundation on normally consolidated soft soil

The design of safe foundations for caissons dykes in an open sea environment

sitting on normally consolidated soft silty and silty clay deposits of low plasticity poses a significant geotechnical challenge. The case described illustrates the difficulties for a proper evaluation of the safety factor against global (or bearing capacity) failure under caisson self-weight and wave loading.

5.11.2 Strength changes due to caisson loading

The following aspects should be accounted for in an analysis of global or bearing capacity type of failure:

- The protocol of caisson sinking and subsequent weight increase.
- The consolidation process under the history of caisson increase in weight.
- The strength increase induced by consolidation.
- The forces induced by wave action under the design storm.
- The risk of soil liquefaction under repeated loading (if foundation soils are prone to liquefaction; see Fig. 5.10).

A step-by-step procedure to consider this sequence of events has been described in this chapter. The analysis of the consolidation process has required the development of a closed form solution for the one-dimensional consolidation equations under a general parabolic initial excess pore pressure.

5.11.3 Undrained vs drained analysis

In low permeability soft soils, the most critical limiting condition is an undrained failure. In this case, the external failure loads are linearly related to the undrained strength. This implies that safety factors, calculated as the ratio of failure and applied loads or as the necessary reduction coefficient of the field undrained strength in order to reach strict equilibrium under the actual external loads should be identical. This is not the case if drained strengths are involved (for instance, if a granular embankment is significantly affected by the critical failure).

5.11.4 Evolution of undrained strength

The initial profile of undrained strength of a normally consolidated deep layer of soil (a linear increase of c_u with depth) is substantially modified during the caisson-induced consolidation process. If upward drainage is allowed (a common case), the undrained strength will initially decrease with depth and eventually it will increase again, beyond a certain depth, when the geostatic stress distribution dominates again the profile. Bearing capacity analyses should be able to include these variations for a proper estimation of the evolution of safety with time. Limit theorems of plasticity offer this possibility at a limited calculation effort.

5.11.5 Spatial distribution of c_u controls mode of failure

The critical failure mechanism is controlled by the spatial distribution of c_u. A linear increase of c_u with depth results in shallower mechanisms. A reduction of strength with depth calls for deeper failure mechanisms.

5.11.6 Type of loading and the failure mechanism

Under pure vertical load (self-weight) and a linearly increasing c_u with depth, a double symmetric mechanism with respect to the axis of loading is the most critical one. However, if horizontal loads are introduced, the double symmetric mechanism in no longer possible and a non-symmetric failure mechanism has to be considered.

5.11.7 Alternative definitions of safety factor

Safety factors may be defined in alternative ways. Whenever possible, the classical definition used in limit equilibrium analysis (ratio of field to mobilized strength) should be preferred. The use of partial safety factors (for drained cohesion and friction coefficient) falls into this category. However, the nature of some loading conditions or, indeed, of the failure mechanisms (a relevant example is the failure mode by overturning of walls, which essentially does not involve the foundation soil strength) may require a different formulation. A natural choice is to compare failure loads and actual loads. One example has been given in the section when examining the caisson safety subjected to wave loading and caisson weight. Two warnings may be issued:

- Alternative definitions of safety factor are possible when comparing failure loads and actual loads. Different numerical values of the safety factor reflect the choice made, although the risk of failure should remain unique.
- Safety factors based on strength reduction (as in limit analysis) or in a comparison of loads, are widely different in drained analysis (because of the highly nonlinear relation between failure loads and drained strength parameters) although the risk of failure remains unique.

5.11.8 Defining soil liquefaction conditions

Liquefaction conditions were defined by means of a cyclic interaction diagram. It combines, in a purely experimental criterion, the static, maintained, or averaged stress ratio, the cyclic stress ratio and the number of applied stress cycles which marks the onset of liquefaction conditions. Such a diagram was available for the deltaic silty foundation soils of the caissons.

5.11.9 Simplified analysis of liquefaction

The cyclic interaction diagram has inspired a simplified procedure to analyze liquefaction under field conditions. Shear stresses in the foundation soil were calculated for the permanent and cyclic caisson loading through available closed form solutions in elasticity. The normalizing effective vertical stress was derived from the consolidation analysis. Once the stress ratios are calculated under the caisson, the cyclic interaction diagram provides the liquefied or non-liquefied areas. It was found that liquefaction takes place on both sides of the caisson, under and beyond caisson edges, and at depths that reach the caisson width.

5.11.10 The flexibility of upper bound calculation

The flexibility and capabilities of the upper bound procedure were demonstrated when the liquefied zones were integrated into a failure analysis of the caisson once liquefaction had occurred. A substantial reduction of failure load was calculated for a reasonable estimation of post-liquefaction undrained strength.

5.11.11 Failure mechanism

After the failure caissons were found tilted, their cap displaced in the seaward direction. The failure mechanism implies that both the caisson weight and the wave forces performed a positive work, balanced by the internal dissipation in the soil. No evidence of overturning induced by wave forces was found.

5.12 Advanced Topics

Vertical caisson failures were collected and discussed by Oumeraci (1994). The author describes the history of design and construction of vertical breakwaters and identifies the causes of failures. However, the field information in most cases is very limited especially as far as soil conditions are concerned. He concludes that forces induced by irregular breaking waves are of special concern and are probably a main reason for the observed failures. Concerning the role of the foundation soil, he observes that scour and erosion at the toe of the structures has often been observed. But major failures are probably associated with pore pressure build-up during cyclic loading and eventually with a full or partial liquefaction of the foundation soils. Unlike earthquake loading, wave action is characterized by long time periods (low frequency of loading), a relatively large number of loading applications, and by a sequence of fast wave impacts if a broken wave hits the wall. Once the soil is liquefied or maintains a certain level of pore water overpressure, failure may occur by a critical slip failure mode.

It has also been observed that the direct wave action on the sea bottom may induce the accumulation of excess pore pressures, a phenomenon which may lead to soil instability. Damage of some marine structures has been attributed to this phenomenon which has been reviewed by Jeng (1998, 2001) and Jeng and Lin (2000). Most of the studies refer to sand beds of high porosity. Excess pore pressures eventually dissipate after the wave action and the soil will consolidate, increasing the resistance to a new significant storm.

The irregular wave pattern originated in the vicinity of a vertical wall has also been associated with observed damage. Not only the cyclic loading but the stress rotation experienced by the soil may induce liquefaction (Sassa and Sekiguchi, 2001).

However, the stress changes induced by the wave loading on the marine structures are significantly larger than the (direct) wave-induced loading on the sea bottom (de Groot *et al*., 2006). This was also the conclusion of large-scale laboratory experiments reported by Kudella *et al*. (2006).

The phenomenon of soil liquefaction has received much attention in geotechnical literature. Most of the experimental information is driven by earthquake research. A comprehensive description of liquefaction behaviour was

provided by Ishihara (1993) and Youd and Idriss (2001).

Model testing has provided further insight into the mechanisms of caisson behaviour under wave loading. Scaled model testing under normal gravitational conditions cannot reproduce the stress conditions prevailing at a prototype scale under the foundation and they can hardly reproduce liquefaction behaviour. The type of failure observed in these tests (seaward motion of caisson top) is not supported by some field observations, including the failure reported here.

Centrifuge testing is a powerful tool to study caisson performance under repeated wave loading. Tests have reported by Rowe and Craig (1976), Van der Poel and de Groot (1998) and by Zhang *et al*. (2009). They all report the behaviour of caissons founded on sand beds. Mechanisms of caisson failure by tilting towards the sea direction have been found. Softening and erosion of the sand in the vicinity of the caisson heel, as well as large liquefied zones beneath the caisson edge, have been proposed by these authors. These studies as well as laboratory cyclic shear test on sands, indicate that reversal and irregular shear loading enhances soil liquefaction (if compared with non-reversal regular cyclic loading).

Appendix 5.1 Hydrodynamic Loads on Caisson

The model proposed by Goda (1985) allows transforming wave heights into loads on the structure once the wave height (H_s), wave period (T), and the wave direction are known. In the analyzed case, $H_s = 4.5$ m, $T = 9$ s and the incident angle of the wave with respect to a line perpendicular to the structure, ϑ, is essentially zero. Figure A5.1a shows the pressure distribution according to Goda (1985). The wave load has two components: a trapezoidal excess pressure distribution on the exposed wall defined by the values P_1, P_2, P_3 and P_4, the run up height, η^*, and geometric parameters, and an uplift triangular pressure distribution on the caisson base defined by the value of P_0. The values of the geometric parameters are also indicated in the figure.

The Goda´s formulae are written as

$$\eta^* = 0.75\left(1+\cos\beta\right)H_D\,,$$

$$P_1 = 0.5\left(1+\cos\beta\right)\left[\alpha_1+\alpha_2\cos^2\beta\right]\gamma_w H_D,$$

$$P_2 = \frac{P_1}{\cosh\left(\dfrac{2\pi h}{L}\right)},$$

$$P_3 = \alpha_1 P_1,$$

$$P_4 = P_1\left(1-\frac{h_c}{\eta^*}\right),$$

$$P_0 = 0.5\left(1+\cos\beta\right)\alpha_1\alpha_3\gamma_w H_D,$$

with the coefficients expressed as

$$\alpha_1 = 0.6 + \frac{1}{2}\left[\frac{4\pi h/L}{\sinh\left(4\pi h/L\right)}\right]^2,$$

$$\alpha_2 = \min\left\{\frac{h_b - d}{3h_b}\frac{H_D^2}{d^2}; \frac{2d}{H_D}\right\},$$

$$\alpha_3 = 1 - \frac{h'}{h}\left(1 - \frac{1}{\cosh\left(\frac{2\pi h}{L}\right)}\right).$$

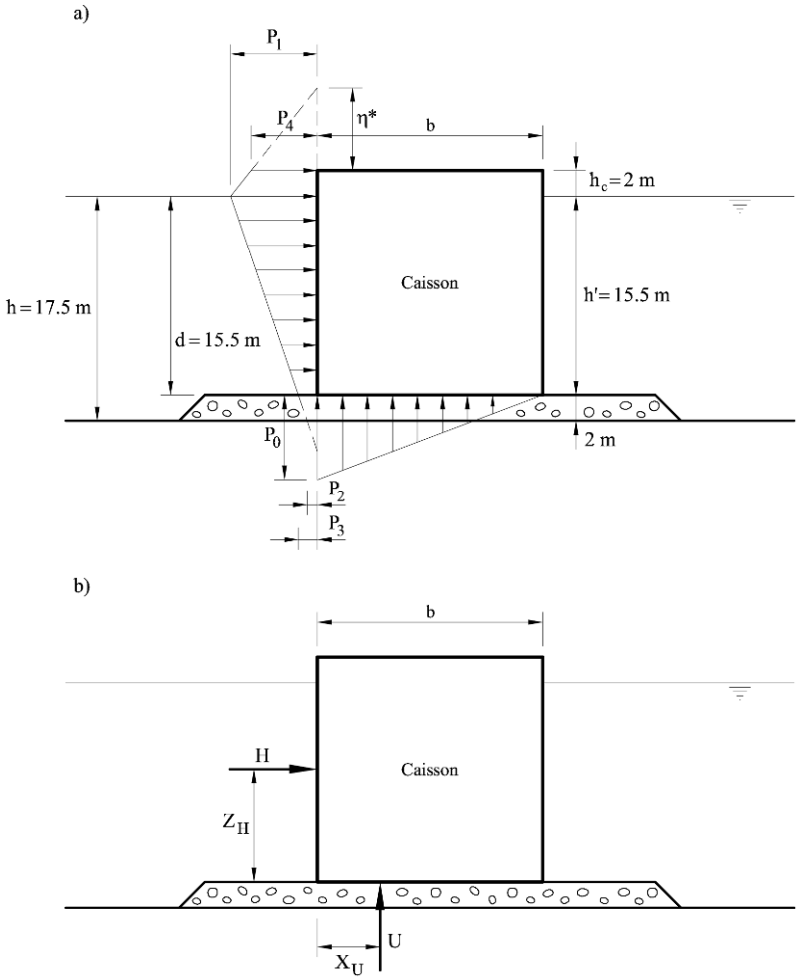

Figure A5.1 (a) Goda's pressure distribution and (b) equivalent concentrated forces.

γ_w is the specific weight of the water (= 10 kN/m^3). The required basic parameters of swell and their values are

$$\beta = \vartheta + 15^\circ = 15^\circ,$$

$$h_b = h + 5 \cdot H_{1/3} \tan\theta = 17.5 + 0 = 17.5 \text{ m},$$

$$L_0 = \frac{gT^2}{2\pi} = \frac{9.8 \cdot 9^2}{2\pi} = 126.34 \text{ m},$$

$$H_{1/250} = 1.8 H_{1/3} \approx 1.8 H_s,$$

$$H_b = 0.17 L_0 \left[1 - \exp\left(-1.5 \frac{\pi h_b}{L_0} \left(1 + 15 \left(\tan\theta \right)^{2/3} \right) \right) \right] =$$

$$= 0.17 \cdot 126.34 \left[1 - \exp\left(-1.5 \frac{\pi \cdot 17.5}{126.34} \right) \right] = 10.30,$$

$$H_D = \min\left\{ H_{1/250}; H_b \right\} = \min\left\{ 1.8 \cdot 4.5; 10.30 \right\} = 8.1,$$

$$L = \frac{gT^2}{2\pi} \tanh\left(\frac{2\pi}{L} h \right) = \frac{9.8 \cdot 9^2}{2\pi} \tanh\left(\frac{2\pi}{L} 17.5 \right) \quad \rightarrow \quad L = 78.19 \text{ m},$$

with these values, $\alpha_1 = 0.657$, $\alpha_2 = 0.01$ and $\alpha_3 = 0.524$ and $P_1 = 53$ kN/m, $P_2 = 24.5$ kN/m, $P_3 = 34.8$ kN/m, $P_4 = 44.2$ kN/m, and $P_0 = 27.4$ kN/m.

Once the pore pressure distribution is calculated, the equivalent forces and their position (Fig. A5.1b) can be calculated as

$$H = \frac{1}{2}\left(P_1 + P_3 \right) h' + \frac{1}{2}\left(P_1 + P_4 \right) h_c = 778.7 \text{ kN/m},$$

$$Z_H = 9.3 \text{ m},$$

$$U = P_0 \frac{b}{2} = 267.4 \text{ kN/m},$$

$$X_U = \frac{b}{3} = 6.5 \text{ m}.$$

References

Alonso, E.E. and Gens, A. (1999) Geotechnical design and construction of breakwaters. Bilbao Harbour (Invited Lecture). *Proceedings of the 12th European Conference on Soil Mechanics and Geotechnical Engineering.* Amsterdam, 1, 489 – 510.

Alonso, E.E. and Krizek, R.J. (1975) Consolidation of randomly heterogeneous clay strata. *Transportation Research Record* 548, 30 – 47.

Davis, E.H. and Booker, J.R. (1973) The effect of increasing strength with depth on the bearing capacity of clays. *Géotechnique* 23 (4), 551 – 563.

Davis, E.H. and Poulos, H.G. (1972) Rate of settlement under two- and three-dimensional conditions. *Géotechnique* 22 (1), 95 – 114.

Goda, Y. (1985) *Random Seas and Design of Maritime Structures*. University of Tokyo Press, Tokyo.

de Groot, M.B., Bolton, M.D., Foray, P., Meijers, P., Palmer, A.C., Sandven, R., Sawicki, A. and The, T.C. (2006). Physics of liquefaction phenomena around marine structures. *Journal of Waterway, Port, Coastal, and Ocean Engineering* 132 (4), 227 – 243.

Ishihara, K. (1993) Liquefaction and flow failure during earthquakes. *Géotechnique* 43 (3), 351 – 415.

Jeng, D.S. (1998) Wave-induced seabed response in a crossanisotropic seabed in front of a breakwater: an analytical solution. *Ocean Engineering* 25 (1), 49 − 67.

Jeng, D.S. (2001) Mechanism of the wave-induced seabed instability in the vicinity of a breakwater: a review. *Ocean Engineering* 28, 537 – 570.

Jeng, D.S. and Lin, Y.S. (2000) Poroelastic analysis of the wave-sea interaction problem. *Computers and Geotechnics* 26, 43 – 64.

Kudella, M., Oumeraci, H., de Groot, M.B. and Meijers, P. (2006) Large-scale Experiments on pore pressure generation underneath a caisson breakwater. *Journal of Waterway, Port, Coastal, and Ocean Engineering* 132 (4), 310 – 324.

Lunne, T., Robertson, P.K. and Powell, J.J.M. (1997) *Cone Penetration Testing in Geotechnical Practice*. Blackie Academic/Chapman and Hall, E&FN Spon, London.

NGI (2002) *Report on DSS Tests*. Port Authority. Barcelona.

Olson, S.M. and Stark, T.D. (2002) Liquefied strength ratio from liquefaction flow failure case histories. *Canadian Geotechnical Journal* 39, 629 – 647.

Oumeraci, H. (1994). Review and analysis of vertical breakwater failures-lessons learned. *Coastal Engineering* 22, 3 – 29.

Potts, D. and Zdravkovic, L. (1999) *Finite Element Analysis in Geotechnical Engineering: Volume I*, *Theory*. Telford Publishing, London.

Poulos, H.G. and Davis, E.H. (1973) *Elastic Solutions for Soil and Rock Mechanics*. Wiley. New York.

Rowe, P.W. and Craig, W.H. (1976) Studies of offshore caissons founded on Ostercheelde sand. *Design and construction of offshore structures*, ICE, London, 49 – 60.

Sassa, S. and Sekiguchi, H. (2001). Analysis of wave-induced liquefaction of sand beds. *Géotechnique* 51 (2), 115 – 126

Seed, R.B., Cetin, K.O., Moss, R.E.S., Kammerer, A.M., Wu, J., Pestana, J.M., Riemer, M.F., Sancio, R.B., Bray, J.D., Kayen, R.E. and Faris, A. (2003) Recent advances in soil liquefaction engineering: a unified and consistent framework. *Proceedings of the 26th Annual ASCE Los Angeles Geotechnical Spring Seminar, Keynote Presentation*, H.M.S. Queen Mary, Long Beach, California. 71 pp.

Van der Poel, J.T. and de Groot, M.B. (1998) Cyclic load tests on a caisson breakwater placed on sand. *Proceedings of the International Conference Centrifuge 98* 1, 403 – 408

Wood, D.M. (1990) *Soil Behaviour and Critical State Soil Mechanics.* Cambridge University Press, Cambridge.

Youd, T.L. and Idriss, I.M. (2001) Liquefaction resistance of soils: summary

report from the 1996 NCEER and 1998 NCEER/NSF workshops on evaluation of liquefaction resistance of soils. *ASCE Journal of Geotechnical and Geo-Environmental Engineering* 127 (10), 297 – 313.

Zhang, X.Y., Lee, F.H. and Leung, C.F. (2009) Response of caisson breakwater subjected to repeated impulsive loading. *Géotechnique* 59 (1), 3 – 16.